



저작자표시-비영리-변경금지 2.0 대한민국

이용자는 아래의 조건을 따르는 경우에 한하여 자유롭게

- 이 저작물을 복제, 배포, 전송, 전시, 공연 및 방송할 수 있습니다.

다음과 같은 조건을 따라야 합니다:



저작자표시. 귀하는 원저작자를 표시하여야 합니다.



비영리. 귀하는 이 저작물을 영리 목적으로 이용할 수 없습니다.



변경금지. 귀하는 이 저작물을 개작, 변형 또는 가공할 수 없습니다.

- 귀하는, 이 저작물의 재이용이나 배포의 경우, 이 저작물에 적용된 이용허락조건을 명확하게 나타내어야 합니다.
- 저작권자로부터 별도의 허가를 받으면 이러한 조건들은 적용되지 않습니다.

저작권법에 따른 이용자의 권리는 위의 내용에 의하여 영향을 받지 않습니다.

이것은 [이용허락규약\(Legal Code\)](#)을 이해하기 쉽게 요약한 것입니다.

[Disclaimer](#)

공학박사학위논문

**Bio-inspired design and fabrication for
multiscale reversible interlocking**

자연모사 기반 멀티스케일 가역적 체결 시스템의 설계 및 제작

2012 년 8 월

서울대학교 대학원

기계항공공학부

방 창 현

Bio-inspired design and fabrication for multiscale reversible interlocking

자연모사 기반 멀티스케일 가역적 체결 시스템의 설계 및 제작

지도교수 서 갑 양

이 논문을 공학박사 학위논문으로 제출함

2012년 6월

서울대학교 대학원

기계항공공학부

방 창 현

방창현의 공학박사 학위논문을 인준함

2012년 6월

위원장 : 최 만 수 (인)
부위원장 : 서 갑 양 (인)
위원 : 안 성 훈 (인)
위원 : 권 성 훈 (인)
위원 : 유 필 진 (인)



Abstract

In this thesis, we describe the bio-inspired design and fabrication using the wing locking device of beetles for exploitation to form a reversible interlocker and flexible and multiplex sensor. The binding of reversible interlocking is based on van der Waals force between high aspect-ratio polymer hairs. Multiscale analysis for reversibility and directionality of interlocking is investigated with structural parameters. Based on van der Waals-assisted interlocking, flexible skin-attachable sensor is demonstrated by utilizing of mechanically interlocking in a reversible, directional manner.

Firstly, we present that the wing locking device of beetles can be exploited to form a reversible interlocker based on van der Waals force-assisted binding between high aspect-ratio polymer hairs. Such a reversible interlocking is inspired from the wing-locking device of beetle where densely-populated microhairs (termed microtrichia) on the cuticular surface form numerous hair-to-hair contacts to maximize lateral shear adhesion. We found that the interlocking is mediated by non-retarded van der Waals forces, which can be significantly amplified owing to the presence of high-density micro- or nanohairs. Especially, the maximum shear locking force of $\sim 40 \text{ N/cm}^2$ was observed for the nanopillar arrays of 50 nm radius and 1 μm height ($\text{AR} = 10$). The measured shear locking forces depend on geometric parameters as well as material rigidity of polymer hairs, in good

agreement with a simple theory based on force balance and hair-merging probability.

From the bio-inspired and reversible interlocker, we analyzed preload-dependent reversible interlocking between regularly-arrayed, high aspect-ratio (AR) polymer micro- and nanofibers. We fabricated various high AR, vertical micro- and nanopillars on flexible substrate and investigated the shear locking force with different preloads ($0.1 \sim 10 \text{ N/cm}^2$). A simple theoretical model is developed based on the competition between van der Waals (VdW) attraction and deflection forces of pillars, which can explain the preload-dependent maximum deflection, tilting angle, and total shear adhesion force.

Next, we investigated bi-directional, asymmetric interlocking between tilted, high aspect-ratio (AR) micro- and nanohairs utilizing geometry-tunable replica molding and broad ion beam irradiation from the directionality of wing locking device. Using this method, various stooped micro- and nanohair arrays (tilting angle $< 40^\circ$) were formed, and then reversibly interconnected each other to measure the shear locking force. It turned out that the maximum force was as high as $\sim 60 \text{ N/cm}^2$ when the two surfaces were pulled in the reverse direction with respect to the bending angle. The hysteresis in this asymmetric, bi-directional adhesion was measured to be ~ 3 , which was in a good agreement with a simple theoretical model.

Finally based on van der Waals-assisted interlocking, we developed a

highly sensitive, flexible, and multiplex strain gauge sensor by utilizing a single active layer of high aspect-ratio Pt-coated polymeric nanofibers that can mechanically interlock in a reversible, directional manner. The sandwich-assembled, interconnected nanofibers that are supported by thin polydimethylsiloxane (PDMS) layers displayed specific, discernible strain-gauge factors (GF) for multiple sensing stimuli such as pressure, shear, and torsion even from an arbitrary input like finger touch. These GF factors were measured from the change in electrical resistance as a function of applied compressive strain ($\leq 5\%$). Highly repeatable and reproducible responses were observed over multiple cycle tests ($<10,000$ cycle) with excellent on/off switching behaviors. In addition, the assembled device was used to monitor the continuous kinetic motion of a bouncing water droplet on a superhydrophobic surface, as well as the physical force of a heartbeat under different conditions.

Key Words : Biomimetics, Beetle, Wing locking device, Interlocking, Dry adhesive, Asymmetric interlocking, nanohairs, Strain gauge sensor, Skin-attachable device.

Student Number: 2009-31247

Contents

Abstract	i
List of tables	vii
List of figures	viii
Nomenclature	xiv
Chapter 1. Introduction	1
Chapter 2. Multiscale, reversible interlocker using beetle-inspired wing locking device	
2-1. Bio-inspired reversible interlocker using regularly arrayed high aspect-ratio polymer fibers	6
2-1-1. Introduction	6
2-1-2. Experimental	9
2-1-2-1. Mechanism of wing-locking device in beetles	9
2-1-2-2. Fabrication of micro-/nano-hair arrays	9
2-1-2-3. Calculation of Hamaker constants	10
2-1-2-4. Adhesion test	14
2-1-2-5. Detailed derivation of the maximum pairing distance D_p and maximum displacement of hairs D_s	14
2-1-2-6. Detailed derivation of interlocking ratio (ξ_l) and maximum shear force	18

2-1-3. Results and Discussion	19
2-1-4. Summary	33
2-2. Analysis of preload-dependent reversible mechanical interlocking	34
2-2-1. Introduction	34
2-2-2. Experimental	40
2-2-2-1. Simulation	40
2-2-3. Results and Discussion	40
2-2-4. Summary	48

Chapter 3. Beetle-inspired bi-directional, asymmetric interlocking using geometry-tunable nanohairs

3-1. Introduction	49
3-2. Experimental	51
3-2-1. Fabrication of various tilted nanohairs	51
3-2-2. Adhesion tests for bi-direction analysis	51
3-2-3. Detailed derivation of maximum angular displacement of hairs $\Delta \theta_p$	52
3-3. Results and Discussion	54
3-4. Summary	67

Chapter 4. A multiplex, flexible, real-time strain gauge sensor using reversible interlocking of nanofibers

4-1. Introduction	68
4-2. Experimental	71
4-2-1. Fabrication and measurement of multiplex, flexible strain gauge sensors	71
4-3. Results and Discussion	72
4-4. Summary	91
References	92
국문초록	103

List of Tables

- Table 2-1** The parameters for calculation of Hamaker constants
- Table 2-2** Summary of material properties used in the experiment: elastic modulus (E), Hamaker constant (A), and friction coefficient (μ) of PU elastomer, soft PUA, and hard PUA. The three materials are denoted as PU, s-PUA, and h-PUA, respectively, for brevity.

List of Figures

- Figure 1-1.** Functional operation of wing locking device of beetles concerning the underlying mechanism of “*reversible*” and “*directional*” binding via sensing organs for conformal contacts.
- Figure 2-1** (a) Photographs of the wing-locking device of the beetle (*Promethis valgipes*). (b-c) SEM images for microtrichia on the cuticular surface with two different magnifications. (d) Schematic of folding and unfolding states of wing locking device.
- Figure 2-2.** Geometrical descriptions of the interconnected hairs upon a preload and an in-plane stretch. Upper and lower hairs are brought in contact (step 1), and make an initial interlocking by non-retarded van der Waals force (step 2). The hairs are displaced until the interlocking is released (step 3). The first and second panels show vertical and projection views of the hairs in contact, respectively.
- Figure 2-3.** (a) Micro and nanohairs of different radius (50 nm, 1.5 μm , and 15 μm) with three ARs (3,6, and 10). For consistency, all the hairy structures had the same spacing ratio of 3 with the hexagonal packing geometry. (b) Shear adhesion forces of the hairy structures (radius: 50 nm, 1.5 μm , and 15 μm) with three ARs (3, 6, and 10). The inset Cross-sectional SEM images of the interlocked hairs for different radius (50 nm, 1.5 μm , and 15 μm). The red arrows indicate the locations of complete interlocking contacts.
- Figure 2-4.** Optical images of the custom-built equipment for shear adhesion measurement (sample size: $1 \times 1 \text{ cm}^2$ area).
- Figure 2-5.** (a) Optical image of large-area fabrication of 50-nm radius and 1- μm height nanohair arrays ($9 \times 13 \text{ cm}^2$). (b) Example of polymeric nano-fastener showing that a 5.25kg fire extinguisher is supported by $1.5 \times 1.5 \text{ cm}^2$ patches.

- Figure 2-6.** Durability of the nanohair interlocker with multiple cycles of attachment and detachment (> 300 cycles) with or without a thin coating of Pt (5 and 10nm). The nanohair arrays of 50 nm radius and 1 μm were used for the tests.
- Figure 2-7.** (a) Simulation snap shots between upper and lower hairs occurring in four consecutive steps: overlap of the hairs by a preload (step 1), pairing via non-retarded van der Waals attraction (step 2), generation of shear force upon in-plane stretching (step 3), and separation of the hairs above maximum displacement and recovery (step 4). In this simulation, soft PUA nanohairs of 50 nm radius and 1 μm height were used. (b) Schematic for the fabrication of an array of high AR hairy structures via replica molding. The measurement of the maximum shear adhesion force was performed with a series of steps (preload, in-plane stretch, and detachment by peeling off).
- Figure 2-8.** (a, b) Interlocking operating zones for 50 nm radius and 1 μm height hairs (a) and for 1.5 μm and 15 μm radius microhairs (b). The lower and upper limits are marked as dotted lines with different colors for each AR.
- Figure 2-9.** (a) Schematic of folding and unfolding states of the wing-locking device of beetle (*Promethis valgipes*) and SEM image for microtrichia on the cuticular surface. (b) Illustration of beetle-inspired interlocking structures with upper and lower fiber arrays. (c) Sequences of interlocking step: i) overlapping by a preload (Step 1), ii) pairing of the fibers by VdW interactions (Step 2), and iii) distortion of the fibers upon application of an in-plane stretch in the shear direction (Step 3).
- Figure 2-10.** (a-b) SEM images of microfiber (3 μm diameter with AR of 10) (a) and nanofiber arrays (100nm diameter with AR of 10) (b). (c-d) Measurement of shear adhesion forces of paired microfiber (c) and nanofiber arrays (d) as compared to gecko-like contact (hair-to-flat surface) (see the inset of c). (e) Cross-sectional SEM images of preload-dependent interlocking between nanofiber arrays (1, 5, and 10 N/cm^2), indicating overlap ratios of ~ 50 , ~ 60 , and ~ 70 %, respectively.

- Figure 2-11.** Simulation snap shots for single paired hairs using ABAQUS 6.9-1 program. When the shear load exceeds the VdW force, the hairs are separated and recoverd their original shape and internal stress (different colors denote different internal stress levels): = (a) 0.3, (b) 0.6, and (c) 0.9.
- Figure 2-12.** Plots of (a) F_{vdw} , F_{def} , (b) θ_p , and (c) D_s of single paired fibers and (d) F_{shear} as a function of $\alpha_{overlap}$.
- Figure 3-1.** (a) Illustration of the actual wing locking device of beetle (*Promethis valgipes*) along with the corresponding SEM images, in which tilted β -keratin microtrichia on the cuticular surface of hind wing and those on the insect body are interlocked. (b) Illustration of folding and unfolding states of the wing locking device. (c) Illustration of directional, asymmetric shear force in the angled (+) and the reverse (-) directions.
- Figure 3-2.** (a-b) SEM images of the as-prepared vertical PU elastomer hairs of 1.5- μm radius, 30- μm height (SR = 3) with hexagonal layout (a) and the same microfibers after oblique broad ion beam irradiation (b) Large-area (i) and magnified views (ii) are shown for each sample. (c) Illustration of reversible cycle of attachment and detachment for shear adhesion tests. (d) Measurement of shear adhesion forces for vertical and asymmetric interlocking in the (+) and (-) directions.
- Figure 3-3.** SEM images for geometry-controlled nanofiber arrays. (a) Vertical nanohair arrays. (b-d) Various tilted nanohairs by oblique broad ion beam irradiation: (b) $\delta = 15^\circ$, (c) 30° , and (d) 40° , respectively. (e, f) Cross-sectional SEM images of paired nanohairs for (e) vertical and (f) tilted nanohairs. Here, the geometry of nanohairs is the same: 50 nm radius, 1 μm height, and SR = 3 with hexagonal layout.
- Figure 3-4.** (a-b) Illustrations for step-by-step events of bi-directional, asymmetric interlocking of single paired nanofibers in the (a) angled (+) and (b) reverse (-) directions. First, the upper and lower tilted nanofibers are paired (step 1), bended to the

maximum angular displacement ($\Delta \theta_p$) before separation (step 2), and finally separated by external shear force (step 3).

Figure 3-5. (a-b) Measurement of shear adhesion forces with various tilting angles in the (a) angled (+) and (b) reverse (−) directions. (c) Plots of theoretical shear adhesion forces as a function of δ in the angled (+) and reverse (−) directions. (d) Comparison of the measured adhesion hysteresis with the theory.

Figure 3-6. Demonstration of directional, asymmetric adhesion with two different pendulums. Two pendulums are supported by $0.8 \times 0.8 \text{ cm}^2$ patches with 3 kg for − direction (a) and 1 kg for + direction (b).

Figure 3-7. Demonstration of the utility as a simple fastener to hold a laptop computer on a $\sim 50^\circ$ slope surface with $1 \times 1 \text{ cm}^2$ patches.

Figure 4-1. Multiplex, flexible strain gauge sensor based on the reversible interlocking of Pt-coated polymer nanofibers. (a) Schematic for the assembly and operation of a flexible sensor layer sandwiched between thin PDMS supports ($\sim 500 \mu\text{m}$ thickness each). (b) Photograph showing the flexibility of the assembled sensor. (c) SEM image of a dense array of 50-nm radius nanohairs with $\text{AR} = 10$. (d) Schematic illustrations of the pressure, shear, and torsion loads and their possible geometric distortions of the paired hairs. (e) Operation of a flexible sensor layer via recording of resistance change (Roff: unloading, Ron: loading).

Figure 4-2. (a) Graph showing the reduction of shear adhesion force with the increase of Pt coating thickness. (b) I-V curves for various Pt-coated nano-interlockers where the 20 nm Pt-coated assembly showed a sufficiently low resistance ($\sim 0.6 \text{ ohm/mm}$) for stable Ohmic-like contact as well as a large shear adhesion force of $\sim 10 \text{ N/cm}^2$. (c) Photograph of an electric connector made of Pt-coated nanofiber interlocks without PDMS sealing.

Figure 4-3. Photograph showing the detailed detection setup with a computer-based user interface via an NI Digital Multimeter (PXI-1033) for measuring the resistance differences, and an

LK-Navigator interface via an LKG 30-KEYENCE laser displacement sensor for recording the applied strains.

- Figure 4-4.** Electric characterizations of the sensor in response to pressure, shear, and torsion loads. Plots showing the difference of the electrical resistance ($R_{\text{off}} - R_{\text{on}}$) for three different mechanical loads of pressure (a), shear (d), and torsion (g) along with changes in the electrical resistance ratio as a function of applied strain for pressure (b), shear (e), and torsion (h). The corresponding SEM images on the right panel (c, f, and i) show structural displacement as a result of each physical load. The GFs were measured from the slope of each plot: ~ 11.45 (pressure), ~ 0.75 (shear), and ~ 8.53 (torsion). The error bars represent the standard deviations.
- Figure 4-5.** (a-c) Plots showing the detailed I-V curves for three different mechanical loadings: pressure (a), shear, (b) and torsion (c).
- Figure 4-6.** Measurement of highly sensitive, multiplex, and real-time signals (a) Schematic illustration of the measurement set-up (see also Figure S4a for details). (b) Multiple-cycle tests ($< 10,000$ cycles) with repeating loading-unloading of pressure in the range of $0 \sim 1500$ Pa. (c-e) Frequency responses to various input signals as a function of time (pressure input frequency: 1 Hz): 1 Hz (c), 5 Hz (d), and 10 Hz (e).
- Figure 4-7.** (a) Photograph of the resistance sensing set-up, which consists of a force controller, a piezoelectric strain gauge sensor, and a computer-based resistance analyzing interface with 100 Hz recording. (b) Plots of $R_{\text{off}} - R_{\text{on}}$ as a function of time (pressure input frequency: 1 Hz) for various applied pressures ($0 \sim 1000$ Pa). As shown, the noise level was distinguishable even for a minimum detectable pressure of ~ 5 Pa.
- Figure 4-8.** (a) Hysteresis of output electric signal for an input pressure of ~ 550 Pa with 1 Hz force frequency. (b) Comparison of input pressure and output signal for an abrupt step input from 0 to 1500 Pa, showing a response lag time of < 0.05 s.
- Figure 4-9.** Fabrication of a sensor network to measure spatial distributions

of an input pressure. (a) The schematic of a real-time, high-sensitivity measurement of the dynamic motion of a bouncing water droplet ($20\ \mu\text{l}$) $\sim 5\ \text{cm}$ above from a superhydrophobic surface. (the inset SEM image [ref. 37]) (b) The corresponding snapshots from a high-speed camera are shown. (c) The difference in the electrical resistance ($R_{\text{off}} - R_{\text{on}}$) for the duration of $\sim 0.4\ \text{sec}$. (d) Photograph showing the skin-attachable sensor right above the artery of the wrist. (e) Measurement of the physical force of a heartbeat under normal (~ 60 beats per min with an average intensity of $\sim 100\ \text{Pa}$) and exercise conditions (~ 100 beats per min with an average intensity of $300\sim 400\ \text{Pa}$). (f) Plots showing the detection and decoupling of pressure, shear, and torsion loads with each time-dependent signal pattern of resistance ratio and applied compressive strain as a function of time. (g) Example for the decoupling of an arbitrary finger touch with pressure, shear, and torsion.

Figure 4-10. Fabrication of a sensor network to measure spatial distributions of an input pressure. (a) Photograph of a fabricated sensor network of 64 pixels over an area of $8 \times 5\ \text{cm}^2$. (b) Schematic of a circuit design. (c-d) Images of device with two lady beetles placed on two locations for pressure sensing: tilted (c) and top views (d), respectively. (e) The resulting two-dimensional intensity profile measured by mapping of the pixel signals.

Nomenclature

n	Refractive index
k	Boltzmann constant
T	Absolute temperature
h	Planck constant
d	Polymer thickness
E	elastic modulus
A	Hamaker constant
F_f	Friction force
F_{vdw}	Van der Waals force
F_{shear}	Total shear adhesion
R	Radius of hairs
l_0	Length of hairs

Greek Symbols

ϵ_x	Dielectric constant
ν_e	Absorption frequency
ϵ_r	Permittivity
α	Contact area
μ	Friction coefficient
θ	Tilting angle of paired hairs
ρ	Density of hair
$\gamma_{spacing}$	Spacing ratio of hair (SR)
$\gamma_{packing}$	Packing ratio of hair
ω	geometric angle of lay-out

ϕ_{area}	Area-covering ratio of paired hairs
ζ_l	Interlocking ratio
$\alpha_{overlap}$	Overlapping ratio
θ_p	Maximum titled angle of paired hairs
δ	Initial tilting angle of hairs
ε	Applied strain
ν	Poisson's ratio
Subscripts	
D_s	Maximum displacement of paired hairs
l	Overlapping length of paired hairs
D_0	Cut-off distance of paired hairs
VdW	Van der Waal force of paired hairs
H	Adhesion hysteresis of +, and – direction
GF	Gauge factor for pressure, shear, and torsion
ΔR	Resistance difference ($\Delta R = R_{off} - R_{on}$)

Chapter 1. Introduction

The efforts to learn and take inspiration from nature have impacted virtually on every scientific area, leading to biomimetic robots, sensors, and materials. [1-5] Reversible binding or interlocking is another attractive feature that nature can provide, which is enabled by a number of different intermolecular (van der Waals force or hydrogen bonds) and electric forces. Examples are found in many biological systems, including the motion of white blood cell on endothelial layer, ligand-receptor bonds, and cell-cell junction. In these examples, the binding is regulated by chemical nature of surface functional groups in such a way that use of a different material leads to a different characteristic of reversible bonding.

In addition, nature has created unique structural devices with specially designed physical structures such as interlocking between “hooks” and “loops” in burdock’s seeds (now commonly used in fabric Velcro) [6] and wing-to-body locking device in beetles [7]. The latter device is operated by bringing densely-populated micro-hairs (termed microtrichia) on the cuticular surface in contact. This interlocking is adapted to fix the wing of insects by maximizing lateral shear friction while minimizing vertical lift-off during numerous cycles of folding and unfolding states. Despite some earlier observations on the existence of wing locking devices in beetles, several issues have not been explored concerning the underlying mechanism of “*reversible*” and “*directional*” binding via sensing organs for conformal contacts as shown in **Figure 1-1**.

Unlike inorganic nanowires and CNTs, the geometry (e.g., length and width), layout density, and material property of polymer hairs can be tuned precisely so as to tailor adhesion force of mechanical interlocking. In addition, it appears that a layered interlocking device provides optimal operating conditions for shear adhesion since the contact is made via numerous tiny hairs present on two flexible surfaces and the lift-off is extremely simple and effortless by peeling off one of layers in contact. Furthermore, regularly titled asymmetric corn-shape microhairs are observed in the wing locking device, whose functionality in reversible attachment has remained unexplored. For further extension of its potential applications, underlying mechanism of interlocking binding via sensing organs can shed light on multi-functional sensor devices. Despite the potential and high-performance of these devices, a wearable, multiplex skin sensor still presents challenges because a large-area fabrication of the integrated device with nanomaterial assemblies (e.g., transistors, nanowires or nanotubes) would be, in many cases, complicated, expensive and minimally reproducible

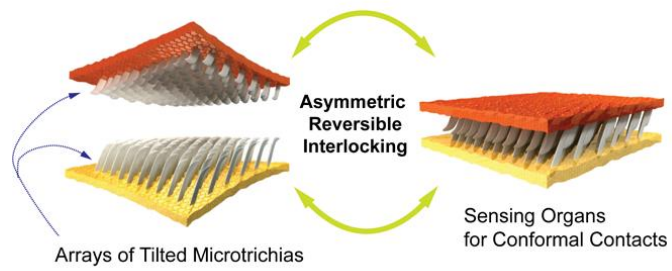
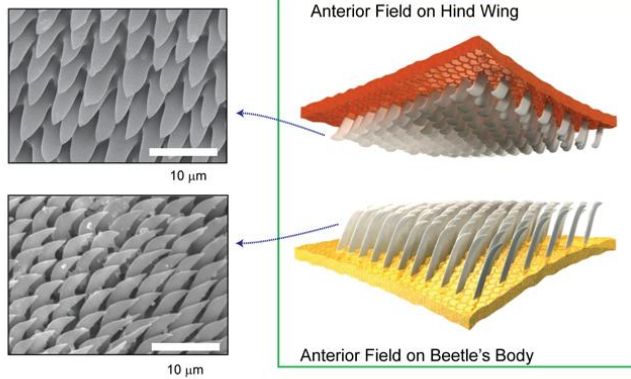


Figure 1-1. Functional operation of wing locking device of beetles concerning the underlying mechanism of “reversible” and “directional” binding via sensing organs for conformal contacts.

In *Chapter 2*, we have presented a robust, reversible interlocking system inspired from the wing locking device of beetles. Experimental and theoretical results demonstrated that the interlocking is mediated by non-retarded van der Waals forces among high-AR hairy structures, resulting in a significantly high locking force in the shear direction ($\sim 40 \text{ N/cm}^2$) and easy lift-off in the normal direction. In contrast to other reversible binding systems, the current interlocking mechanism does not involve any complicated physical structures (e.g., hooks or loops) or surface chemical moieties, allowing for a simple, yet efficient route to reversible interlocker in a noise-less and cost-effective manner. Furthermore, we have presented the preload-dependent reversible mechanical interlocking between regularly-arrayed, high-AR polymer fiber arrays. Our experimental and theoretical studies demonstrated that the shear adhesion force is strongly affected by the applied preload ($0.1\sim 10 \text{ N/cm}^2$). We have confirmed the increase of overlap ratio with the increase of preload, which supports the linear tendency of locking force as a function of preload.

In *Chapter 3*, we describe bi-directional, asymmetric interlocking between tilted, high aspect-ratio (AR) micro- and nanohairs utilizing geometry-tunable replica molding and broad ion beam irradiation. Using this method, various stooped micro- and nanohair arrays (tilting angle, $\delta < 40^\circ$) were formed, and then reversibly interconnected each other to measure the shear locking force. It turned out that the maximum force was as high as $\sim 60 \text{ N/cm}^2$ when the two surfaces were pulled in the reverse direction with respect to the bending angle. The hysteresis in

this asymmetric, bi-directional adhesion was measured to be ~ 3 , which was in a good agreement with a simple theoretical model.

In *Chapter 4*, we have presented a highly flexible, multiplex, real-time sensor based on reversible mechanical interlockers between Pt-coated, high-AR nanofibers. In contrast to other detection systems, the current nano-interlocking mechanism does not involve any complex integrated nanomaterial assemblies or layered arrays, allowing for a simple, cheap, yet robust sensing platform for high-performance, large-area strain gauge sensors. Using the assembled strain sensor, we measured three different mechanical loads in the form of normal pressure, shear, and torsion with high sensitivity and wide dynamic range. In addition, the output signals were highly repeatable and reproducible over multiple cycle tests (< 10000 cycles) with excellent on/off switching behaviors. For potential applications, the assembled device was used to detect the dynamic motion of a small bouncing water droplet and the physical force of a heartbeat, shedding light on its potential use in real-time monitoring, skin-like wearable electronics or implantable medical devices.

Chapter 2. Multiscale, reversible Interlocker using beetle-inspired wing locking device

2-1. Bio-inspired reversible interlocker using regularly arrayed high aspect-ratio polymer fibers

2-1-1. Introduction

The wing-locking device in beetles is operated by bringing densely-populated micro-hairs (termed microtrichia) on the cuticular surface in contact. This interlocking is adapted to fix the wing of insects by maximizing lateral shear friction while minimizing vertical lift-off during numerous cycles of folding and unfolding states. Despite some earlier observations on the existence of wing locking devices in beetles, [7] several issues have not been explored concerning the underlying mechanism of reversible binding and its potential applications to flexible interlocker.

Recently, core-shell type nanowires and CNT-based carbon forests have been introduced as a permanent or reversible adhesive between two surfaces. [8, 9] We report here that regularly ordered high aspect-ratio (AR) polymer fibers can also be used as a reversible interlocker owing to the amplification of van der Waals forces. Unlike inorganic nanowires and CNTs, the geometry (e.g., length and width), layout density, and material property of polymer hairs can be tuned

precisely so as to tailor adhesion force of mechanical interlocking. In addition, it appears that a layered interlocking device provides optimal operating conditions for shear adhesion since the contact is made via numerous tiny hairs present on two flexible surfaces and the lift-off is extremely simple and effortless by peeling off one of layers in contact.

To investigate multiscale interlocking behaviors of high-AR hairs (or pillars) we used three polyurethane (PU)-based materials of different rigidity (elastic modulus: 3 MPa ~ 10 GPa). Using these materials, various pillar arrays were fabricated with three different radii (50 nm, 1.5 μm , and 15 μm) and aspect ratios (3, 6, and 10) (total of 27 experimental sets). We found that the interlocking is mediated by non-retarded van der Waals forces, which can be significantly amplified owing to the presence of high-density micro- or nanohairs. Especially, the maximum shear locking force of $\sim 40 \text{ N/cm}^2$ was observed for the nanopillar arrays of 50 nm radius and 1 μm height (AR = 10), which appears the best among the polymer adhesives reported to date.

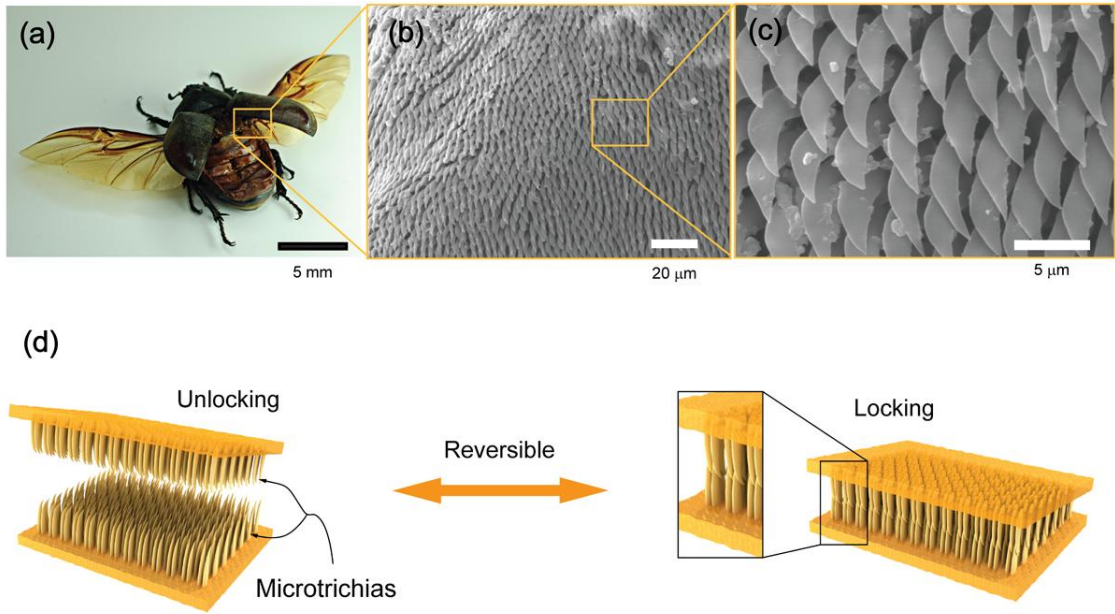


Figure 2-1. (a) Photographs of the wing-locking device of the beetle (*Promethis valgipes*). (b-c) SEM images for microtrichia on the cuticular surface with two different magnifications. (d) Schematic of folding and unfolding states of wing locking device.

2-1-2. Experimental

2-1-2-1. Mechanism of wing-locking device in beetles

The wing-locking device in beetles normally contains five surfaces covered by outgrowths on the body and eight surfaces on the wings with unique surface sculptures.[22] Each of these functional surfaces prevents movement of the closed wing in some preferred direction. More specifically, the corn-shaped microtrichia in hindwing locking pad and counterpart of hemelytra (the boxed area in **Figure 2-1a**) are interlocked to resist lateral sliding motion of the body (**Figure 2-1d**). The loading force is mainly generated by muscles for elastic microtrichia with selective pressure. Counterpart may be preloaded by a muscular contraction and act as a spring-loaded contacting surface. The detachment occurs gradually towards one direction for minimizing muscular force.

2-1-2-2. Fabrication of micro-/nano-hair arrays

The silicon master molds with micro- and nanoholes were prepared by photolithography and subsequent reactive ion etching. The molds were treated with a fluorinated-SAM solution ((tridecafluoro-1,1,2,2-tetrahydrooctyl)-trichlorosilane:FOTCS, Gelest Corp.) diluted to 0.03 M in anhydrous heptane (Samchon Corp.) in Ar chamber. The surface-treated master molds were annealed at 120°C for 20 min. Drops of PU Elastomer (PU), or PUA prepolymers (s-PUA; PUA MINS 311 RM, h-PUA; PUA MINS 301 RM) purchased from the Minuta

Tech, Korea were dispensed onto the master and a PET film (50 μm) was slightly pressed against the liquid drop for it to be used as a supporting backplane. After preparing a polymer replica by UV exposure and mold removal, the PUA replica was additionally exposed to UV for several hours for complete curing. Details on the synthesis and characterization of the PUA polymers can be found elsewhere. [10, 11] For the fabrication of hair arrays, three types of micro- and nanoscale pillar structures were used with the above three polymer materials: i) 50 nm radius nanohairs of 300 nm, 600 nm, and 1 μm height, ii) 1.5 μm radius with 9 μm , 18 μm , and 27 μm height, and iii) 15 μm radius with 90 μm , 180 μm , and 270 μm height. In total, 27 experimental sets were prepared and used for SEM measurements and adhesion tests.

2-1-2-3. Calculation of Hamaker constants

According to Lifshitz theory, the Hamaker constant can be determined by dielectric constant (ϵ_x) and refractive index (n) of each material, yielding [12]

$$A = A_{v=0} + A_{v>0} = \frac{3}{4} kT \left(\frac{\epsilon_1 - \epsilon_3}{\epsilon_1 + \epsilon_3} \right)^2 + \frac{3h\nu_e}{16\sqrt{2}} \frac{(n_1^2 - n_3^2)^2}{(n_1^2 + n_3^2)^{3/2}} \quad (1)$$

where k is the Boltzmann constant ($1.38 \times 10^{-23} \text{ JK}^{-1}$), T is the absolute temperature, h is the Planck constant ($6.63 \times 10^{-34} \text{ Js}$), and ν_e is the material's absorption frequency ($1.2 \times 10^{15} \text{ s}^{-1}$). The permittivity (ϵ_r) is calculated from the capacitance measurement: $C = \epsilon_r \epsilon_0 \alpha / d$ where ϵ_0 is the vacuum permittivity

(8.85×10^{-12} F/m), α is the contact area, and d is the polymer thickness (LCR Bridge 2400, Electro Scientific Industries, Inc.) in **Table 2-1**. Refractive indices (n) of polyurethane elastomer (PU) and soft/hard PUA (s-PUA and h-PUA) are 1.46 and 1.50, respectively, from the literature. [13, 14]

Table 2-1. The parameters for calculation of Hamaker constants

	PU		s-PUA		h-PUA	
Frequency (Hz)	120	1000	120	1000	120	1000
Measured Capacitance (C) (nF)	11.7	5.8	7.08	6.03	11.4	10.7
Contact area (α)(mm²)	1	1	1	1	1	1
Thickness of polymer layer (d) (μm)	10.01	10.01	9.0	9.0	4.0	4.0
Calculated permittivity (ϵ_r)	17.32	12.47	7.19	6.12	5.16	4.83

Table 2-2. Summary of material properties used in the experiment: elastic modulus (E), Hamaker constant (A), and friction coefficient (μ) of PU elastomer, soft PUA, and hard PUA. The three materials are denoted as PU, s-PUA, and h-PUA, respectively, for brevity.

Material	Elastic modulus (E)	Hamaker constant (A)	Friction coefficient (μ)
PU	~ 3 Mpa	5.71×10^{-20} J	0.12
s-PUA	~ 19.8 Mpa	2.09×10^{-20} J	0.04
h-PUA	350 Mpa ~ 10 Gpa	1.78×10^{-20} J	0.08

2-1-2-4. Adhesion test

The adhesion patch ($1 \times 1 \text{ cm}^2$ area) was attached with a preload of 10 N/cm^2 until a failure occurred. All measurements were repeated at least 10 times at ambient temperature and a relative humidity 50% and average values were used for the plots. Frictional coefficient (μ) was measured by a scratch/wear tester CP-4, CETR.

2-1-2-5. Detailed derivation of the maximum pairing distance D_p and maximum displacement of hairs D_s

When the hairs are brought in contact by an applied load, they are attracted by non-retarded van der Waals forces, forming a reversible contact between the two layers as shown in **Figure 2-2**. Here, the force between the hairs can be written as $F_{vdw} = A\sqrt{R} \cdot l / (16D^{2.5})$, [15] in which A is the Hamaker constant, R is the hair radius, D is the distance between hairs, and l is the overlap length. In the course of interlocking, the deflection of hairs costs the bending energy of upper and lower vertical hairs, which is given by $F_{def} = 48EID / \{(2l_0 - l)^2 (4l_0 + l)\}$ where I is the moment of inertia ($I = \pi \cdot R^4 / 4$, R is the radius of hairs), l_0 is the total length of hairs, and E is the elastic modulus of the polymer material. It is noted that the original beam deflection equation is modified by using the overlap distance l . Then, the maximum pairing distance between hairs D_p can be determined by equating the van der Waals and the hair

deflection forces. Since two hairs are involved in a single contact, one can assume $F_{vdw}(D_p) = 2F_{def}(D_p)$, which gives with expression of overlap ratio ($\alpha_{overlap} (= l/l_0)$) between upper and lower hairs

$$D_p \cong 131\gamma_{aspect} (R\gamma_{aspect})^{1/7} \cdot (A/E)^{2/7} \cdot \{\alpha_{overlap} (2 - \alpha_{overlap})^2 (4 + \alpha_{overlap})\}^{2/7} \quad (2)$$

Here, in case of 70% overlap ratio with 10 N/cm² loads, the maximum pairing distance (D_p) can be obtained

$$D_p \cong 0.47 \bar{\gamma}_{aspect} (R\gamma_{aspect})^{1/7} \cdot (A/E)^{2/7} \quad (3)$$

In order to obtain an expression for the maximum displacement of nanohairs before separation, we can assume the Amonton's first law of friction ($F_f = \mu F_{vdw}$). [16] Additionally, we have to consider the counterbalance force induced by deflection of the tilting angle (θ) of paired hairs. According to the force balance, the interlocked hairs would maintain the merged state until $F_{def} \sin \theta < \mu(F_{vdw} - F_{def} \cos \theta)$ as shown in **Figure 2-2** (setp1, 2, and 3). When $F_{def} \sin \theta = \mu(F_{vdw} - F_{def} \cos \theta)$, the paired hairs would start to be separated. After some algebraic manipulation by Taylor series, one can have maximum displacement of hairs D_s as following procedure

$$\mu \frac{F_{vdw}}{F_{def}} = \theta_p + \mu \quad (4)$$

$$\frac{1.27}{l_0} D_s + \mu \cong \frac{\mu F_{vdw}}{F_{def}} \quad (5)$$

$$D_s \cong \frac{(4 + \alpha_{overlap}) \mu \gamma_{aspect} R}{6} \left[\sqrt{\frac{\alpha_{overlap} (2 - \alpha_{overlap})^2}{\pi D_0^{2.5}} \cdot \frac{\gamma_{aspect}^3}{R^{0.5}} \cdot \frac{A}{\mu E} + 1} - 1 \right] \quad (6)$$

With 70% overlap ratio with 10 N/cm² loads, the maximum pairing distance (D_p) can be expressed

$$D_s \cong 0.783 \mu \gamma_{aspect} R \left[\sqrt{\frac{0.376}{D_0^{2.5}} \cdot \frac{\gamma_{aspect}^3}{R^{0.5}} \cdot \frac{A}{\mu E} + 1} - 1 \right] \quad (7)$$

where $F_{vdw} = A\sqrt{R} \cdot l / (16D_0^{2.5})$. [17] In this derivation, the expressions for the deflection force ($F_{def} = 48EID_s / \{(2l_0 - l)^2(4l_0 + l)\}$) and tilting angle ($\theta = 6D_s / \{(4 + \alpha_{overlap}) \cdot l_0\}$) are used assuming the “part-uniformly distributed load of beam deflection” ($\delta_{max} = wl^4 / 8EI$ and $\theta = wl^3 / 2EI$). [18] Also, the average overlap length is assumed to be $0.7l_0$ from our experimental observations.

Finally after simple approximation with some algebraic manipulation, one can have the maximum displacement (D_s)

$$D_s \cong 5.5 \times 10^4 \frac{(4 + \alpha_{overlap})}{\alpha_{overlap}} \cdot \frac{\mu R}{r_{aspect}^4} \cdot \frac{F_{vdw}}{F_{def}} \quad (8)$$

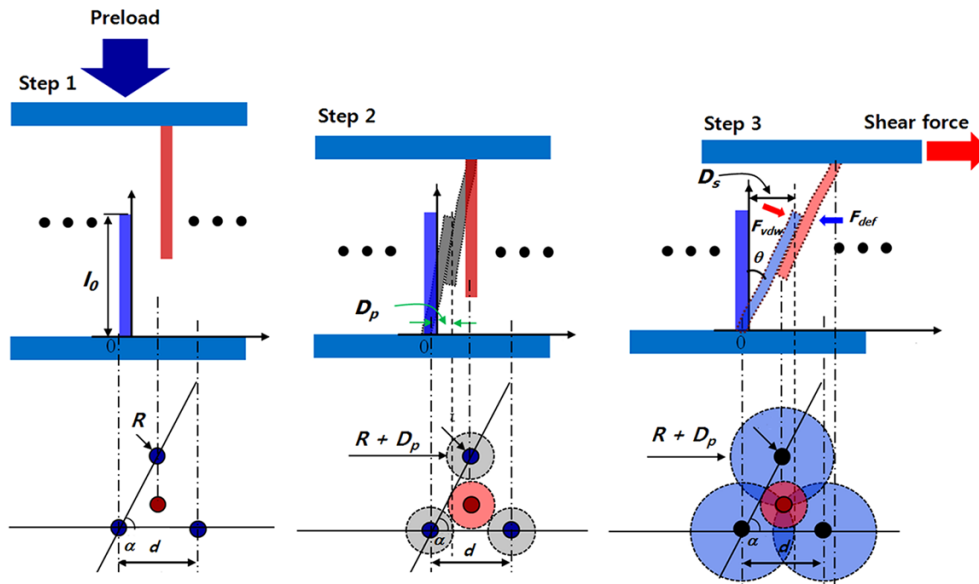


Figure 2-2. Geometrical descriptions of the interconnected hairs upon a preload and an in-plane stretch. Upper and lower hairs are brought in contact (step 1), and make an initial interlocking by non-retarded van der Waals force (step 2). The hairs are displaced until the interlocking is released (step 3). The first and second panels show vertical and projection views of the hairs in contact, respectively.

2-1-2-6 Detailed derivation of interlocking ratio (ξ_l) and maximum shear force

Area ratio (ϕ_{area}) should be larger than unity as shown in below illustrations of **Figure 2-2**

$$\phi_{area} = \frac{\pi(R + D_s)^2}{4R^2(\gamma_{spacing} + 1) \cdot \sin \alpha} > 1 \quad (9)$$

Here, $\gamma_{spacing}$ is the same at 3 and the arrangement angle α is 60° for the hexagonal packing geometry. This lower limit accounts for the maximum hair-merging probability in a misaligned state. Next, the upper limit is given by the geometric consideration, such that the interlocking ratio $\xi_l (= D_s / R)$ should be less than double the interspacing ratio so as to prevent clumping with the bottom substrate. Therefore one can have

$$\sqrt{\frac{4(\gamma_{spacing} + 1) \sin \alpha}{\pi}} - 1 < \xi_l < 2\gamma_{aspect} \quad (10)$$

We predicted the total shear for per unit area (cm^2) by multiplying the hair density ($\#/\text{cm}^2$) to the shear adhesion force per single hair: $F_{shear} = \rho \cdot F_{vdw} \cos \theta$. Here, the hair density can be accurately estimated using the hair spacing ($\gamma_{spacing}$), geometric angle ($\omega = 60^\circ$), and packing ratio:

$$\rho = \left\{ 8R^2(1 + \gamma_{spacing})^2 \sin \alpha \right\}^{-1} \cdot \gamma_{packing}^2 \quad (11)$$

where $\gamma_{packing}$ is 0.7 and 1 for the nanohairs and microhairs, respectively.

2-1-3. Results and Discussion

Figure 2-1a-c shows photographs of the beetle (*Promethis valgipes*) and its anterior field of thorax, which contains dense, hexagonal microhair arrays of approximately 0.9 μm radius and 18 μm height with the spacing ratio (= distance between hairs divided by width) of ~ 3 . When these hairs are interconnected, a high shear locking force is expected to occur as schematized in the left bottom panel of **Figure 2-1d**, while a normal lift-off would be extremely simple and effortless. This wing locking device is highly reversible and does not require additional physical load or surface modification. A close examination in **Figure 2-1c** reveals that the microhairs are slightly bended in one direction, allowing for pointed directionality along a particular spatial axis. The primary function of these microhairs is to reversibly lock the wing of beetles, whose contact is continuously monitored by conjunctive sensory organs (see supporting information for details). In addition, this wing locking device is known to protect delicate flight wings and dehydration of nanopore channels by air drying [7]. The microhairs are made of β -keratin, whose elastic modulus and Hamaker constant were reported to be ~ 2 GPa and $\sim 10 \times 10^{-20}$ J, respectively. [19, 20]

To demonstrate multiscale interlocking behaviors by van der Waals interactions, we tested a variety of hairy structures with different structural dimensions and material properties. After preparing silicon masters with suitable geometry, the polymer hairs were fabricated by replica molding technique. Here, three polymer materials of different rigidity were used: PU (polyurethane

elastomer, elastic modulus: 3 MPa), s-PUA (soft PUA, MINS 301 RM, elastic modulus: 19.8 MPa), and h-PUA (hard PUA, MINS RM 311, elastic modulus: 350 MPa ~ 10 GPa) (see **Table 2-2**). [10, 11] Therefore, the modulus spans three orders of magnitude. Using these materials, various pillar arrays were prepared with the radius ranging from 50 nm to 15 μm (three orders of magnitude difference). For each pillar array, three different ARs (AR = height/diameter, 3, 6, and 10) were used, thus giving the total of 27 experimental sets (see **Figure 2-3** and **Figure 2-4**). The tilted SEM images of replicated polymer structures are shown in **Figure 2-3a**, demonstrating that the structures have high structural fidelity and integrity. Here, each group (column) was classified depending on the radius of hairs, which was 50 nm, 1.5 μm , and 15 μm , respectively. For consistency, all hairy structures had the same spacing ratio of 3 with the hexagonal packing geometry. The interlocking layers could be formed over a large area ($9 \times 13 \text{ cm}^2$) in a single replication step (see **Figure 2-5a**).

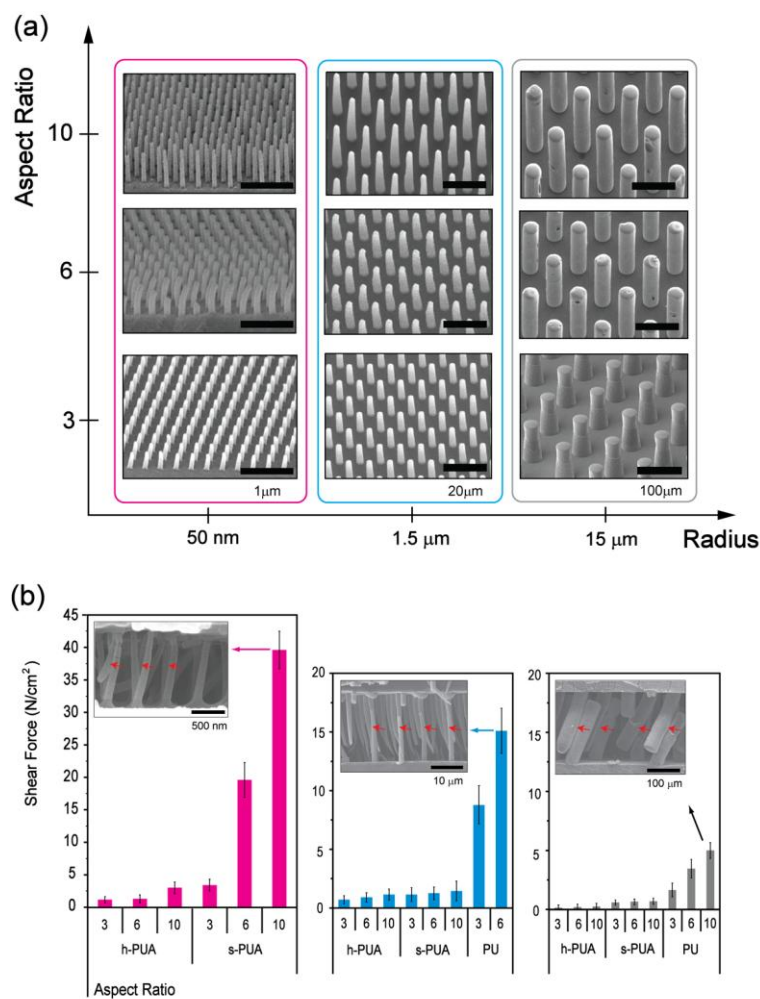


Figure 2-3. (a) Micro and nanohairs of different radius (50 nm, 1.5 μm, and 15 μm) with three ARs (3,6, and 10). For consistency, all the hairy structures had the same spacing ratio of 3 with the hexagonal packing geometry. (b) Shear adhesion forces of the hairy structures (radius: 50 nm, 1.5 μm, and 15 μm) with three ARs (3, 6, and 10). The inset Cross-sectional SEM images of the interlocked hairs for different radius (50 nm, 1.5 μm, and 15 μm). The red arrows indicate the locations of complete interlocking contacts.

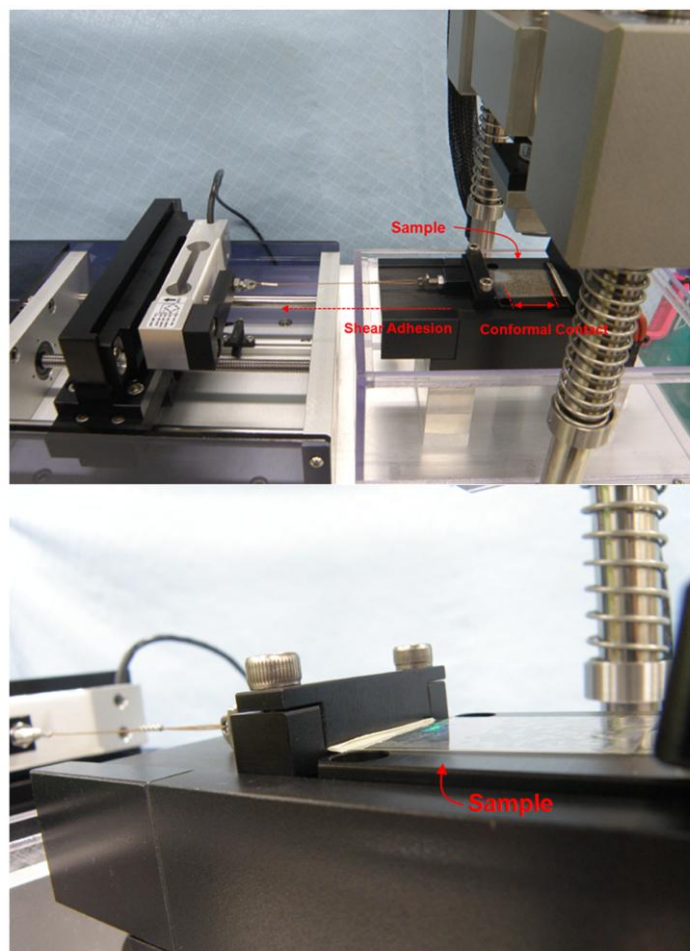


Figure 2-4. Optical images of the custom-built equipment for shear adhesion measurement (sample size: $1 \times 1 \text{ cm}^2$ area).

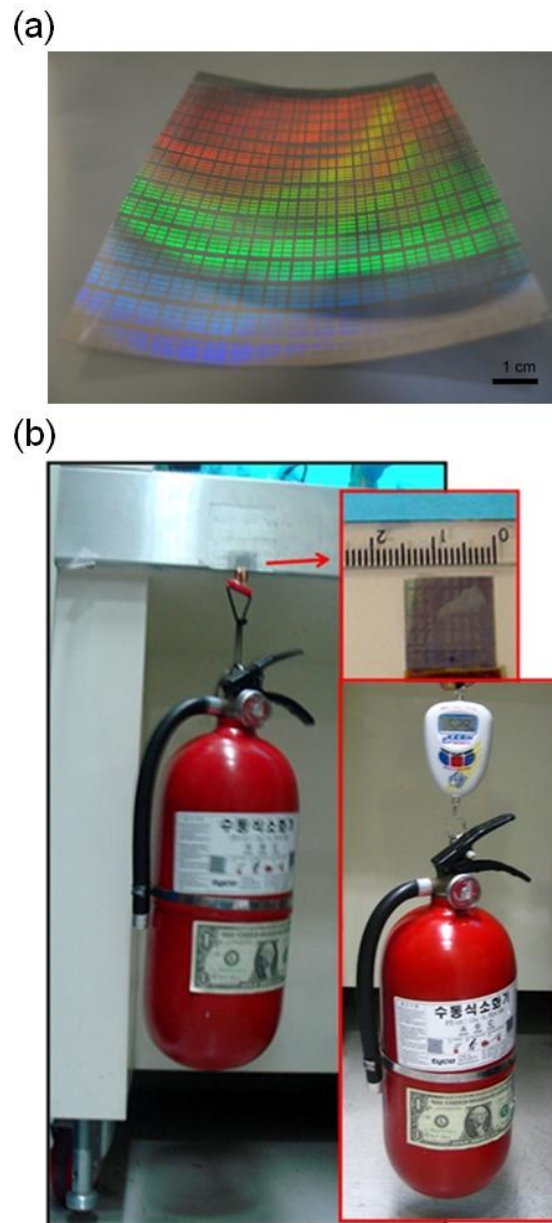


Figure 2-5. (a) Optical image of large-area fabrication of 50-nm radius and 1- μm height nanohair arrays ($9 \times 13 \text{ cm}^2$). (b) Example of polymeric nano-fastener showing that a 5.25kg fire extinguisher is supported by $1.5 \times 1.5 \text{ cm}^2$ patches.

The maximum shear locking forces were measured by custom-built equipment with a preload of 10 N/cm^2 at the relative humidity 50% until a failure occurred (**Figure 2-3b** and **Figure 2-4**). Several notable findings are derived from the figure. First, a smaller radius gives a higher shear force, which was valid for all ARs and mechanical moduli shown in **Figure 2-3b**. Since a small radius is equivalent to a higher hair density and thus a higher number of hair-to-hair interlocking contacts per unit sample area, it is directly related to a higher adhesion force. Second, the shear strength increased with the decrease of elastic modulus and the increase of AR for all hairy structures tested. In particular, nanohairs of 50 nm radius and 1 μm height showed the best shear locking force of $\sim 40 \text{ N/cm}^2$ for intermediate modulus (19.8 MPa), which is presumably the highest shear strength among the polymer-based dry adhesives reported so far (see **Figure 2-5**). [21] For comparison, the maximal adhesion forces of typical fabric Velcro and gecko-like polymer-based dry adhesives were reported to be $\sim 15 \text{ N/cm}^2$ [22] and $\sim 26 \text{ N/cm}^2$ [21], respectively. In contrast, microhairs of 1.5 μm radius and 18 μm height, the scale of which is often found in many insects [7], showed the maximum adhesion of $\sim 17 \text{ N/cm}^2$ for low modulus (3 MPa), suggesting that softer hairs lead to a higher shear adhesion force for a given geometry. Third, the maximum shear adhesion is limited by replication capability of hairy structures. Namely, there is a certain limit in producing high AR structures due to collapse or mating between neighboring hairs. [21] This explains the reason why some shear adhesion data (nanohairs of radius 50 nm and microhairs of radius 1.5 μm) are missing, and nanohairs of the intermediate modulus provided the maximum shear force instead of the elastomer in **Figure 2-3b**. The inset SEM images shown in

Figure 2-3b provides an insight into how the interlocking contact is mediated by multiscale hairy structures. Here, the red arrows indicate the locations where complete interconnections had been made with overlapped hairs. The ratio of the overlapping was estimated to be 65~75% regardless of the rigidity of the hairs, with some broken and misaligned hairs.

Figure 2-6 demonstrates the durability of interlocker using the nanohairs of 50 nm radius and 1 μm height over multiple cycles of attachment and detachment with or without a thin coating of Pt (5 and 10nm). It is noted that these interlocking layers, when mechanically reinforced with a thin metal layer, allow for noise-less and repeatable adhesion over > 300 cycles without significant reduction in adhesion strength.

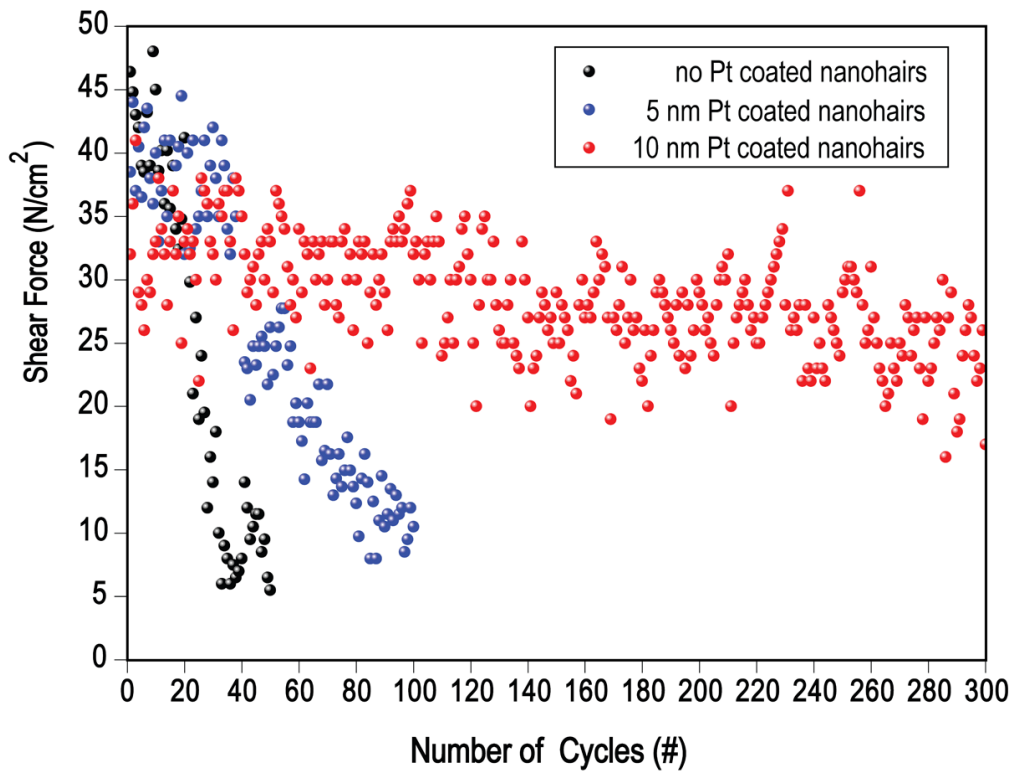


Figure 2-6. Durability of the nanohair interlocker with multiple cycles of attachment and detachment (> 300 cycles) with or without a thin coating of Pt (5 and 10nm). The nanohair arrays of 50 nm radius and 1 μm were used for the tests.

To gain further understanding on multiscale van der Waals-assisted interlocking, we derive a simple theory based on force balance and hair-merging probability. The hair-to-hair interlocking contact would occur in a series of steps (see **Figure 2-7**). When the hairs are brought in contact by an applied load, they are attracted by non-retarded van der Waals forces, [12] forming a reversible contact between the two layers. Here, the force between the hairs can be written as $F_{vdw} = A\sqrt{R} \cdot l / (16D^{2.5})$, [15] in which A is the Hamaker constant, R is the hair radius, D is the distance between hairs, and l is the overlap length. The Hamaker constants of PU elastomer, s-PUA, and h-PUA were calculated to be 5.71×10^{-20} J (A_{PU}), 2.09×10^{-20} J (A_{s-PUA}) and 1.78×10^{-20} J (A_{h-PUA}) in **Table 2-2**. In the course of interlocking, the deflection of hairs costs the bending energy of upper and lower vertical hairs, which is given by $F_{def} = 48EID / \{(2l_0 - l)^2(4l_0 + l)\}$ where I is the moment of inertia ($I = \pi \cdot R^4 / 4$, R is the radius of hairs), l_0 is the total length of hairs, and E is the elastic modulus of the polymer material (see **Table 2-2**). It is noted that the original beam deflection equation is modified by using the overlap distance l . Then, the maximum pairing distance between hairs D_p can be determined by equating the van der Waals and the hair deflection forces. Since two hairs are involved in a single contact, one can assume $F_{vdw}(D_p) = 2F_{def}(D_p)$, which gives

$$D_p \cong 0.475 \gamma_{aspect} (R \gamma_{aspect})^{1/7} \cdot (A/E)^{2/7} \quad (3)$$

where γ_{aspect} is the AR of hairs ($= l_0 / 2R$) and the constant 0.475 originates from the average overlap length of $0.7l_0$ from our experimental observations. Therefore,

the interlocking probability increases with the increase of the AR, hair length, and van der Waals forces, while decreasing with the increase of the modulus of material.

Once the initial contact is made, the maximum displacement of hairs D_s prior to separation can be derived based on force balance and friction law. Since the hairs are now merged, the van der Waals force is described by $F_{vdw} = A\sqrt{R} \cdot l / (16D_0^{2.5})$ [12], in which the cut-off gap distance between hairs D_0 is assumed to be 0.4 nm. [15] After plugging in the tilting angle (θ) of $1.276D_s / l_0$ and applying the force balance $F_{def} \sin \theta = \mu(F_{vdw} - F_{def} \cos \theta)$ with algebraic manipulation, one can have

$$D_s \cong 0.783\mu\gamma_{aspect}R \left[\sqrt{\frac{0.376}{D_0^{2.5}} \cdot \frac{\gamma_{aspect}^3}{R^{0.5}} \cdot \frac{A}{\mu E} + 1} - 1 \right] \quad (7)$$

where μ is the frictional coefficient of each material (**Table 2-2**). Therefore, the maximum deflection is linearly proportional to $R \cdot \gamma_{aspect}$ (or l_0), which is readily understood in terms of geometrical consideration. Additionally, the theoretical shear adhesion force per single hair can be predicted based on the same formulation, yielding $F_{shear} = F_{vdw} \cos \theta$. The maximum shear adhesion is predicted to be $\sim 65\text{N/m}^2$ for the nanohairs of 50 nm radius and 1 μm height, and $\sim 29\text{N/cm}^2$ for the microhairs of 1.5 μm radius and 18 μm height, respectively, which are approximately 1.5 to 2 times higher than the experimental data shown in **Figure 2-3b**. It appears that the interlocking contact is not complete in part due to misalignment of upper and lower hair arrays and some structural defects.

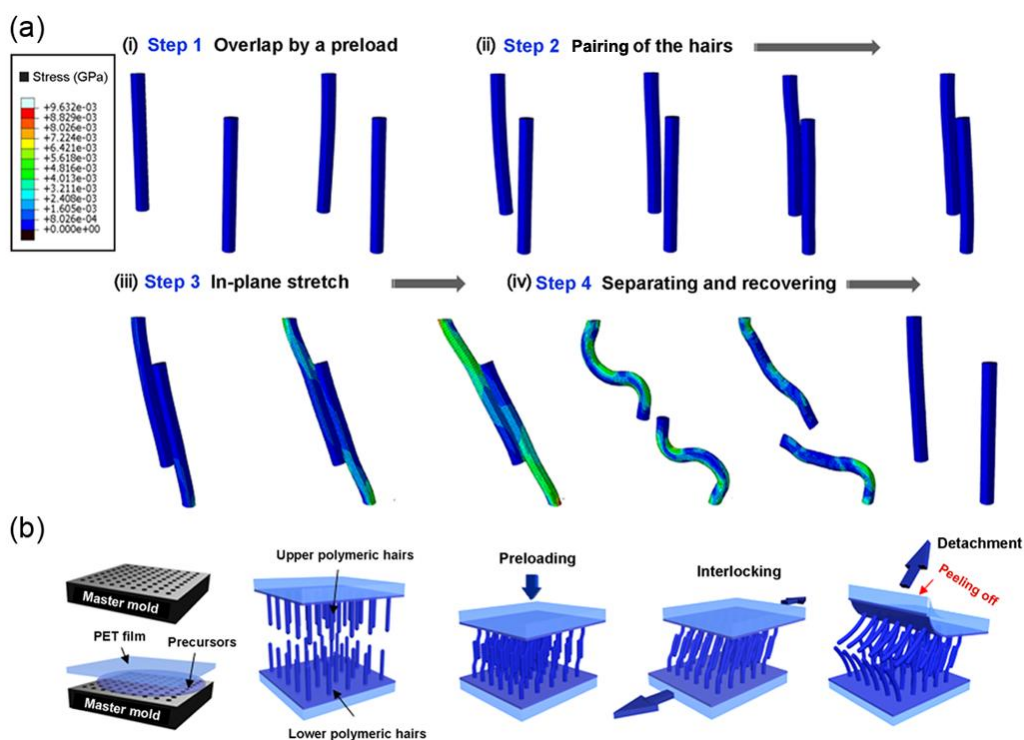


Figure 2-7. (a) Simulation snapshots between upper and lower hairs occurring in four consecutive steps: overlap of the hairs by a preload (step 1), pairing via non-retarded van der Waals attraction (step 2), generation of shear force upon in-plane stretching (step 3), and separation of the hairs above maximum displacement and recovery (step 4). In this simulation, soft PUA nanohairs of 50 nm radius and 1 μm height were used. (b) Schematic for the fabrication of an array of high AR hairy structures via replica molding. The measurement of the maximum shear adhesion force was performed with a series of steps (preload, in-plane stretch, and detachment by peeling off).

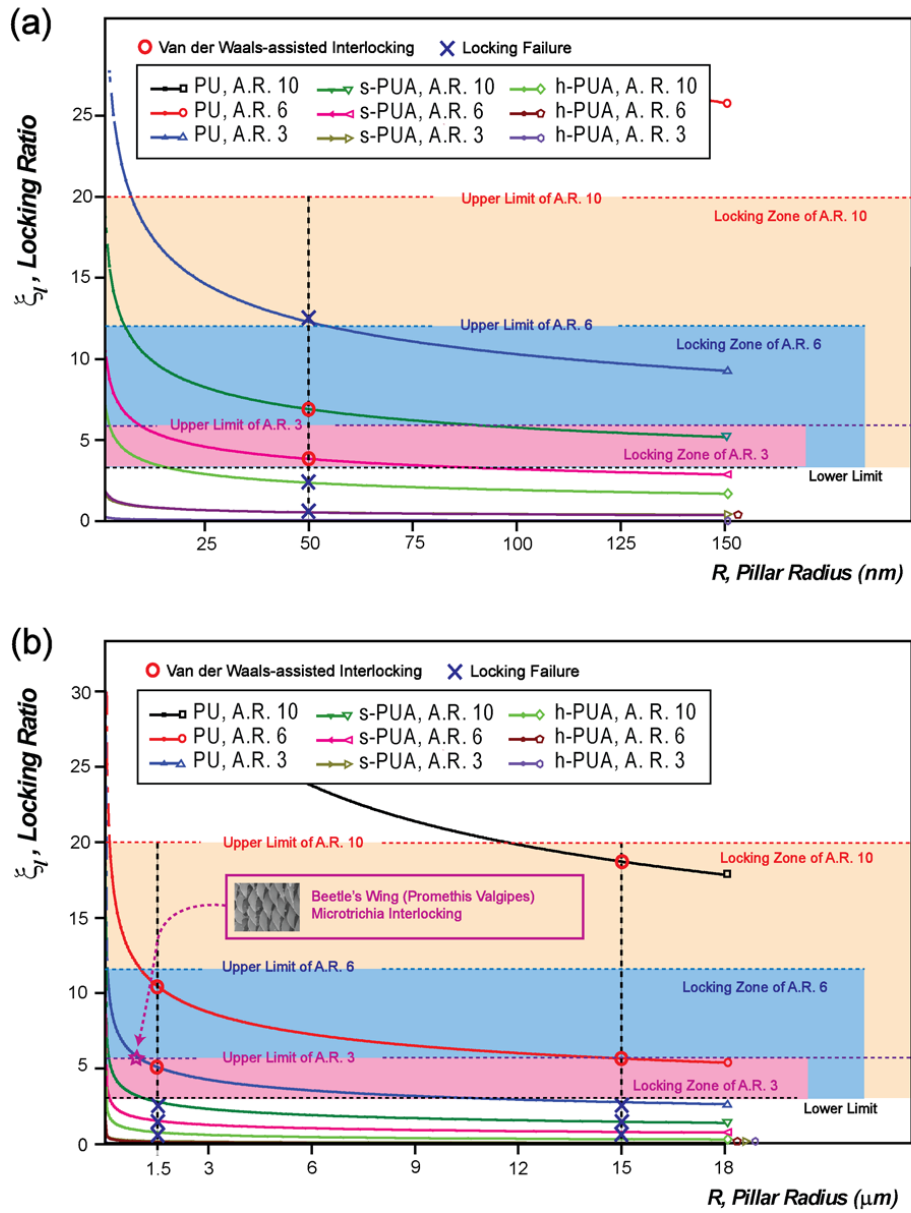


Figure 2-8. (a, b) Interlocking operating zones for 50 nm radius and 1 μm height hairs (a) and for 1.5 μm and 15 μm radius microhairs (b). The lower and upper limits are marked as dotted lines with different colors for each AR.

To judge whether interlocking would take place or not, it is useful to set lower and upper limits of locking criterion. For the hexagonal unit cell arrays with a certain spacing ratio ($\gamma_{spacing} = d/2R$), it can be assumed that D_s should exceed the unit cell distance to contact the neighboring hairs even in a misaligned state. Thus, the lower limit of interlocking setting is derived from the condition where the area ratio (ϕ_{area}) should be larger than unity:

$$\phi_{area} = \frac{\pi(R + D_s)^2}{4R^2(\gamma_{spacing} + 1) \cdot \sin \alpha} > 1 \quad (9)$$

Here, $\gamma_{spacing}$ is the same at 3 and the arrangement angle α is 60° for the hexagonal packing geometry. This lower limit accounts for the maximum hair-merging probability in a misaligned state. Next, the upper limit is given by the geometric consideration, such that the interlocking ratio $\xi_l (= D_s/R)$ should be less than double the interspacing ratio so as to prevent clumping with the bottom substrate. Therefore one can have

$$\sqrt{\frac{4(\gamma_{spacing} + 1)\sin \alpha}{\pi}} - 1 < \xi_l < 2\gamma_{aspect} \quad (10)$$

After inserting appropriate values into the parameters in equations 9 and 10, it follows that $3.20 < \xi_l < 2\gamma_{asp}$. **Figure 2-8** shows the plots of ξ_l against the change of hair radius for each experimental set with corresponding material properties in **Table 2-2**. The lower and upper limits of interlocking are marked as dotted lines with different colors for each AR. As can be seen from the figure, the

existence of van der Waals force-assisted interlocking can be predicted by comparing the interlocking zones with the plots based on equation 10, which is also in excellent agreement with our experimental observations in **Figure 2-3b** as well as the wing locking device of the beetle (*Promethis valgipes*) in **Figure 2-1**. It is noted that the interlocking zone becomes wider as the AR increases for given material rigidity, suggesting that the structures of high AR are advantageous for efficient interlocking.

2-1-4. Summary

We have presented a robust, reversible interlocking system inspired from the wing locking device of beetles. Experimental and theoretical results demonstrated that the interlocking is mediated by non-retarded van der Waals forces among high-AR hairy structures, resulting in a significantly high locking force in the shear direction ($\sim 40 \text{ N/cm}^2$) and easy life-off in the normal direction. In contrast to other reversible binding systems, the current interlocking mechanism does not involve any complicated physical structures (e.g., hooks or loops) or surface chemical moieties, allowing for a simple, yet efficient route to reversible interlocker in a noise-less and cost-effective manner. A simple theory was developed on the basis of force balance and hair-merging probability, which is capable of explaining the maximum shear adhesion and operating zones for various geometrical and material parameters.

2-2. Analysis of preload-dependent reversible mechanical interlocking

2-2-1. Introduction

Recently, a wide range of nature-inspired functional surfaces have been introduced for various applications such as water/oil repellence [23-25], water collection [26], dry adhesion [27-31], structural color [32, 33], and biomedical patch. [34, 35] Multiscale, hierarchical structures are usually found on such surfaces, in which each structure has unique geometry and hierarchy to be useful under different environments for each living organism. Compared to other surfaces, the reversible interlocking property of the beetle's wing-fixation device has recently drawn much attention. [7, 36] A pioneering work was reported by Gorb and coworkers where they found that the wing fixation is operated by bringing numerous microhairs on the cuticular surface in contact, thereby generating a high lateral shear friction while minimizing vertical lift-off. The characteristic of this mechanical interlocking is slightly different from the well-known hook-and-loop formation in burdock's seeds (now commonly used in fabric Velcro), and thus provides an insight into a new binding mechanism towards reversible attachment and detachment.

In addition to beetles, the reversible interlocking system is also found in dragonfly's head arrester consisting of unique fibrillar structures. [37] In both cases, the locking is enabled by reversible fixation between microstructures (known as microtrichia), which are regularly-arrayed, dense micro-fibers on the

cuticular surface. The function of microtrichia fields is reflected in their structural architecture, density, shape, shear or vertical directionality and material properties at interconnecting surfaces.

A variety of useful applications are conceivable based on the above-mentioned reversible interlocking. For example, several research groups reported core-shell type nanowires and CNT-based carbon forests as a permanent or reversible adhesive between surfaces. [38] While the results are interesting and potentially useful to electric connectors, the underlying mechanism of the interlocking is still not clear as the detailed structural analysis has been missing. We fabricated various regularly-arrayed, high-AR polymer fibers made of UV-curable polyurethane acrylate (PUA) materials. In order to assess the effect of structural dimensions and materials properties, we used three PUA materials of different rigidity (elastic modulus: 3 MPa ~ 10 GPa) with various hair radii and ARs, and found that the locking force increased with the decrease of hair radius and modulus and the increase of AR. In particular, the maximum shear locking force of $\sim 40 \text{ N/cm}^2$ was observed for the nanopillar arrays of 50 nm radius and 1 μm height (AR = 10), which was probably the highest adhesion strength among the polymer adhesives in Chapter 2-1.

We report on how the interlocking is mediated by different preloads in views of maximum deflection and angle, and total adhesion force prior to the detachment. It is readily expected that the total adhesion strength would be elevated with increasing the preload. Nonetheless, the degree of overlap between fibers and its respective deformation needs to be understood to accurately describe the interlocking behavior. To this aim, we used two types of high-AR pillars of

PU elastomer (diameter = 3 μm , AR = 10, elastic modulus \sim 3 MPa) and soft PUA (s-PUA, diameter = 100 nm, AR = 10, elastic modulus \sim 19.8 MPa). Measurement of shear adhesion force demonstrated that the locking force was enhanced with the increase of preload for both materials. From the simulation, a typical stick-slip dynamic motion was predicted in response to an in-plane stretch, which can be interpreted as a competition between van der Waals (VdW) and deflection forces. Finally, a simple theoretical model was derived to incorporate the effect of the two competing forces, which was used to explain the preload-dependent behavior of the interconnected fibers.

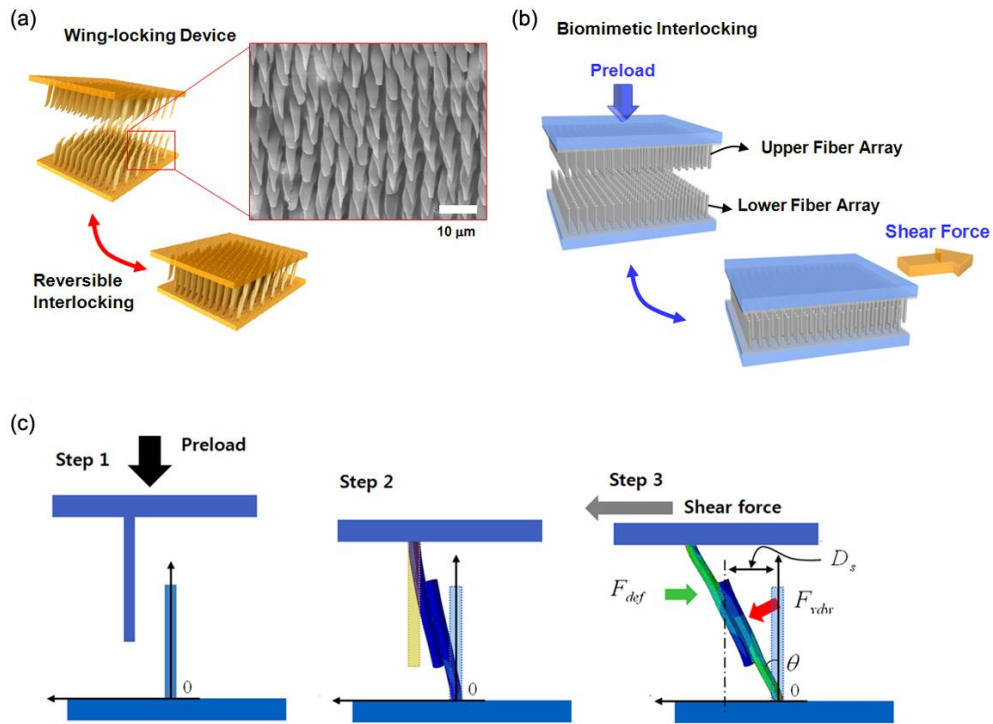


Figure 2-9. (a) Schematic of folding and unfolding states of the wing-locking device of beetle (*Promethis valgipes*) and SEM image for microtrichia on the cuticular surface. (b) Illustration of beetle-inspired interlocking structures with upper and lower fiber arrays. (c) Sequences of interlocking step: i) overlapping by a preload (Step 1), ii) paring of the fibers by VdW interactions (Step 2), and iii) distortion of the fibers upon application of an in-plane stretch in the shear direction (Step 3).

Figure 2-9a shows SEM image of the beetle's wing-fixation microfiber array at its anterior field of thorax (*Promethis valgipes*) and illustrations for the interlocking mechanism. As seen from the image, the fixation unit is composed of dense, hexagonal microhair arrays of approximately 0.9 μm radius and 18 μm height with hexagonal packing (hair-to-hair distance divided by hair diameter ~ 3). Such regularly-arrayed microfibers are interconnected when the upper and lower layers are brought in contact, which in turn generates a high shear locking force against an in-plane stretch (**Figure 2-9a**). Beetles are using these structures when they need to stay on trees or grounds while protecting their large, intricate, and delicate wings. Also, the interlocking of cuticle microstructure made of β -keratin provides effortless folding with high shear adhesion and reversibility. According to previous studies [36], the function of this wing-fixation device is associated with body cleaning, food grinding, air holding, thermoregulation, and filtration with aerodynamically or hydrodynamically active surface. A close examination of SEM image reveals that the shape of microtrichia is tapered along the top with an inclination angle, displaying a pointed directionality towards a particular spatial axis. In contrast, the microfibers used here are straight with a uniform thickness. For better structural similarity, this deviation needs to be addressed in a future study.

Inspired from this wing-locking device, artificial micro- and nanofiber arrays were prepared as shown in **Figure 2-9b**. The upper and lower layers having the identical fiber arrays were interconnected in such a way that numerous hair-to-hair contacts were formed with a certain overlap. Due to some misalignment and collapse of fibers, the configuration of each interlocking would be different from

single to multi-body contacts. As shown shortly, the degree of overlap was turned out to be a function of the applied preload. A schematic shown in **Figure 2-9c** shows the sequences of interlocking step: i) overlapping by a preload (Step 1), ii) pairing of the fibers by VdW interactions (Step 2), and iii) distortion of the fibers upon application of an in-plane stretch in the shear direction (Step 3).

2-2-2. Experimental

2-2-2-1. Simulation

The simulations were performed using the ABAQUS 6.9-1 program (SIMULIA). The following parameter values were used: Young's modulus (E) = 19.8 MPa (PUA MINS 301 RM) and 300 MPa (PUA MINS 311 RM), and Poisson's ratio (ν) = 0.3

2-2-3. Results and Discussion

Figure 2-10a-b shows SEM micrographs of dense micro- and nanofiber arrays formed on flexible PET substrate. These well-defined structures were formed over a large area ($9 \times 13 \text{ cm}^2$) without notable defects. Using these fiber arrays, shear adhesion forces were measured by varying the applied preload in the range of $0.1\sim 10 \text{ N/cm}^2$. As shown in **Figure 2-10c-d**, the interlocking-assisted shear adhesion (hair-to-hair) was compared with the gecko-like adhesion (hair-to-flat surface, see the inset of **Figure 2-10c**). With the increase of preload, the shear adhesion force ranged from 3 to 17 N/cm^2 for the microfiber arrays, whereas it ranged from 3 to 40 N/cm^2 for the nanofiber arrays. For the gecko-like attachment, the adhesion value was usually less than 40% of the interlocking. These observations strongly suggest that the shear adhesion is largely determined by the applied preload.

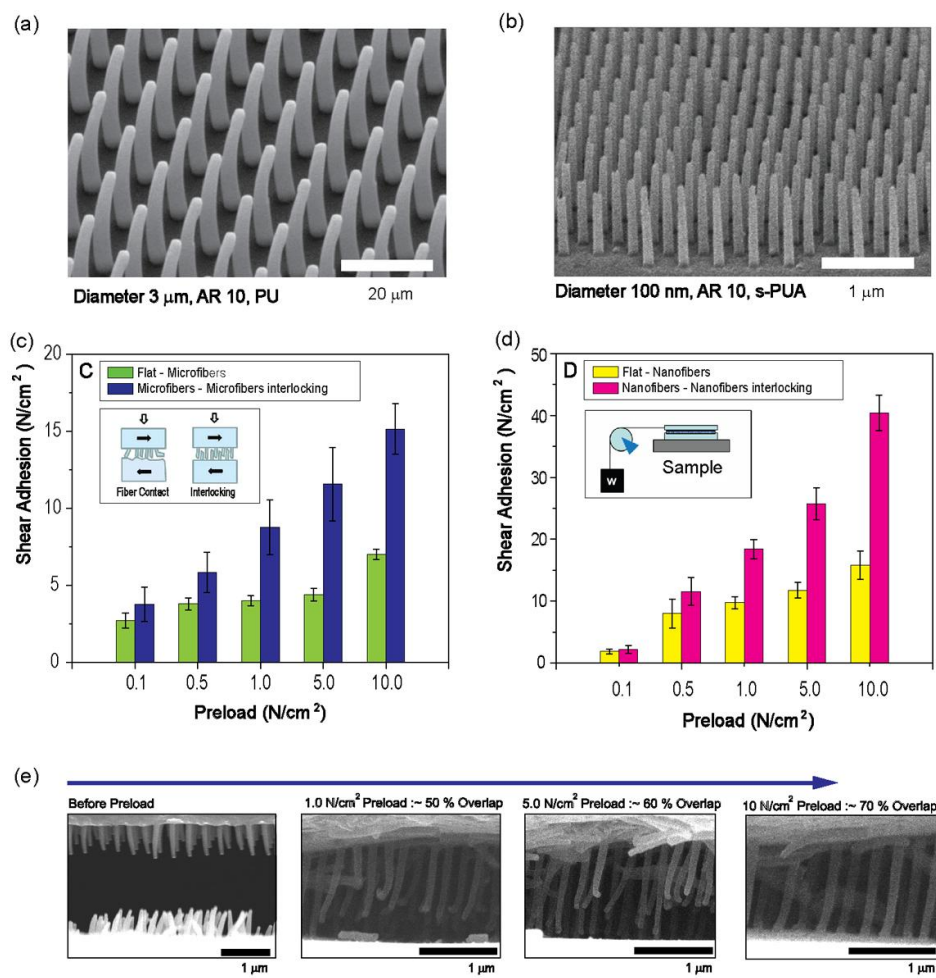


Figure 2-10. (a-b) SEM images of microfiber (3 μm diameter with AR of 10) (a) and nanofiber arrays (100nm diameter with AR of 10) (b). (c-d) Measurement of shear adhesion forces of paired microfiber (c) and nanofiber arrays (d) as compared to gecko-like contact (hair-to-flat surface) (see the inset of c). (e) Cross-sectional SEM images of preload-dependent interlocking between nanofiber arrays (1, 5, and 10 N/cm^2), indicating overlap ratios of \sim 50, \sim 60, and \sim 70 %, respectively.

In order to elaborate on the preload effect, we measured SEM images of interconnected nanofiber arrays with different preloads (1, 5, and 10 N/cm²). As expected, the degree of overlap between upper and lower fibers was dependent on the preload; it ranged from ~50, ~60, and ~70 % in the order of increasing the preload. A further increase of the preload (>10 N/cm²) was not effective, in that the fibers were susceptible to collapse and the overlapping was not improved. A linear dependency was observed for both mechanical contacts but the slope was much higher for the interlocking. Among various structures, the nanofiber array of 50 nm radius and 1 μm height showed a remarkable shear adhesion force as high as ~ 40 N/cm².

To understand the preload-dependent mechanical interlocking of single fiber contacts, a series of simulation snap shots are present in **Figure 2-11** using a multiscale mechanical simulation tool (ABACUS 6.9-1). Here, individual nanohairs of soft PUA (50nm radius and 1μm height) are brought in contact by a preload and then attracted by VdW forces (F_{vdw}) to form a reversible contact. [12] According to the literature, F_{vdw} can be written as [15]

$$F_{vdw} = \frac{A\sqrt{R} \cdot l_0 \cdot \alpha_{overlap}}{16D_0^{2.5}} \quad (12)$$

where A is the Hamaker constant, R is the hair radius, D_0 (0.4 nm) is the distance between hairs, l_0 is the length of hair, and $\alpha_{overlap}(=l/l_0)$ is the overlap ratio between upper and lower hairs. Here, the Hamaker constant of s-PUA is approximated to 2.09×10^{-20} by the measurement of materials properties (see **Table 2-2**). Additionally, from the geometric consideration illustrated in **Figure**

2-9c, one needs to consider the counterbalance by deflection (F_{def}) of hairs, which is given by

$$F_{def} = \frac{48EID_s}{l_0^3 (2 - \alpha_{overlap})^2 (4 + \alpha_{overlap})} \quad (13)$$

where I is the moment of inertia ($I = \pi \cdot R^4 / 4$) and D_S is the maximum displacement length. For simplicity, we assumed the condition of part-uniformly distributed load of beam deflection. [18] As can be seen from the simulation snapshots, the hair-to-hair contact is maintained until the deflection force overcomes the VdW force upon application of an in-plane stretch. In all cases, the well-known stick-slip motion was observed. [16] When the shear load exceeds the VdW force, then the hairs are finally separated and recover their original shape and internal stress (different colors denote different internal stress levels). It is noted that the maximum deflection displacement and angle of paired fibers were highly dependent on the overlap ratio, such that they were lowered with the increase of $\alpha_{overlap}$.

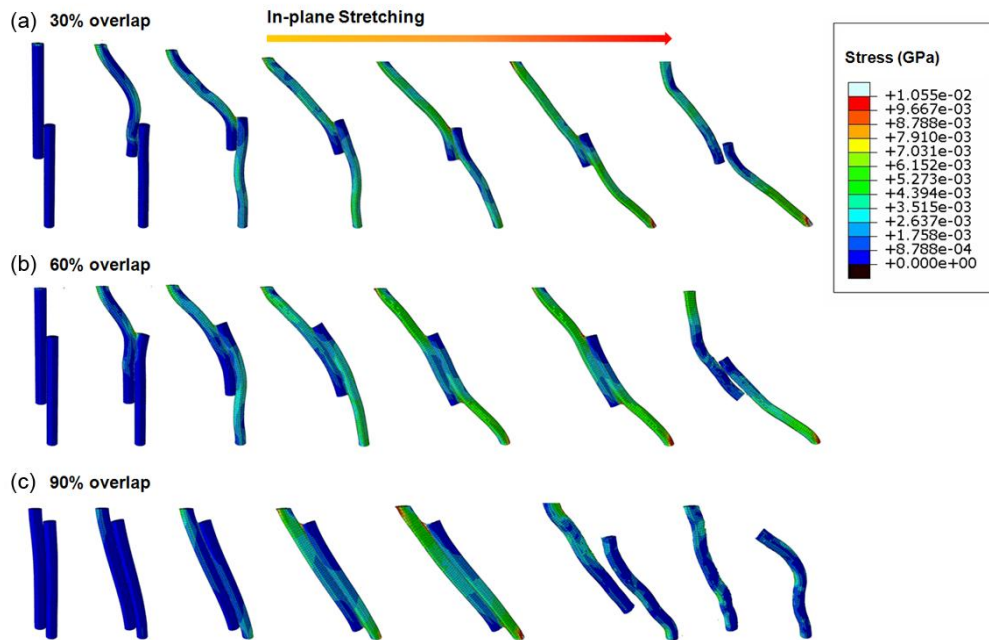


Figure 2-11. Simulation snapshots for single paired hairs using ABAQUS 6.9-1 program. When the shear load exceeds the VdW force, the hairs are separated and recover their original shape and internal stress (different colors denote different internal stress levels): $\alpha_{overlap} =$ (a) 0.3, (b) 0.6, and (c) 0.9.

To obtain an expression for the maximum displacement of paired fibers before separation, we assume the Amonton's first law of friction ($F_{friction} = \mu F_{load}$). [39] According to the force balance, the interlocked hairs would maintain the merged state until $F_{def} \sin \theta < \mu(F_{vdw} - F_{def} \cos \theta)$, where the μ is friction coefficient of materials ($\mu = 0.04$ for s-PUA) and θ is the tilted angle by shear adhesion force. When the dislocating force ($F_{def} \sin \theta$) to the perpendicular direction becomes $\mu(F_{vdw} - F_{def} \cos \theta)$, the paired fibers would be separated, yielding a criterion as

$$F_{def} \sin \theta_p = \mu(F_{vdw} - F_{def} \cos \theta_p) \quad (14)$$

where θ_p is the maximum titled angle via preload and can be simply written as

$$\theta_p = \frac{6D_s}{l_0(4 + \alpha_{overlap})} \quad (15)$$

After some algebraic manipulation, one can have the maximum displacement (D_S):

$$D_S \cong 5.5 \times 10^4 \frac{(4 + \alpha_{overlap})}{\alpha_{overlap}} \cdot \frac{\mu R}{r_{aspect}^4} \cdot \frac{F_{vdw}}{F_{def}} \quad (8)$$

This relation indicates that D_S can be determined by the competition between VdW and deflection forces with friction coefficient μ and the geometric AR ($r_{aspect} = l_0 / 2R$) of fiber arrays that differs from the structural AR of fibers.

Figure 2-12a-c shows plots of forces (F_{vdw} , F_{def}), θ_p , and D_S of single paired fibers as a function of $\alpha_{overlap}$ on the basis of the above equations. For the

calculations, we used nanofiber array of 50 nm radius and 1 μm height. As shown in **Figure 2-12a**, the VdW force is overwhelmingly higher than the deflection force for the entire range of $\alpha_{overlap}$. Once the hairs start to be deflected, the contribution from the dislocating force ($F_{def} \sin \theta$) becomes pronounced and ultimately equals to the friction force of paired hairs ($\mu(F_{vdw} - F_{def} \cos \theta)$). A notable finding here is that both θ_p , and D_S are reduced with the increase of $\alpha_{overlap}$ since a larger deflection force is required for a higher $\alpha_{overlap}$. Similarly, the total shear adhesion force per unit area (cm^2) (F_{shear}) can be derived by multiplying the hair density ($\#/\text{cm}^2$) to the shear adhesion force per single hair:

$$F_{shear} = \rho \cdot F_{vdw} \cos \theta_p \quad (16)$$

Here, the hair density (ρ) was $\sim 1.85 \times 10^9$ from the hair spacing and hexagonal layout used in the experiment. Using the estimated θ_p in **Figure 2-12b**, F_{shear} is plotted as a function of $\alpha_{overlap}$ in **Figure 2-12d**, indicating that the measured maximum shear adhesion ($\sim 40 \text{ N}/\text{cm}^2$) corresponds to $\alpha_{overlap}$ of 70%, in excellent agreement with our experimental observations.

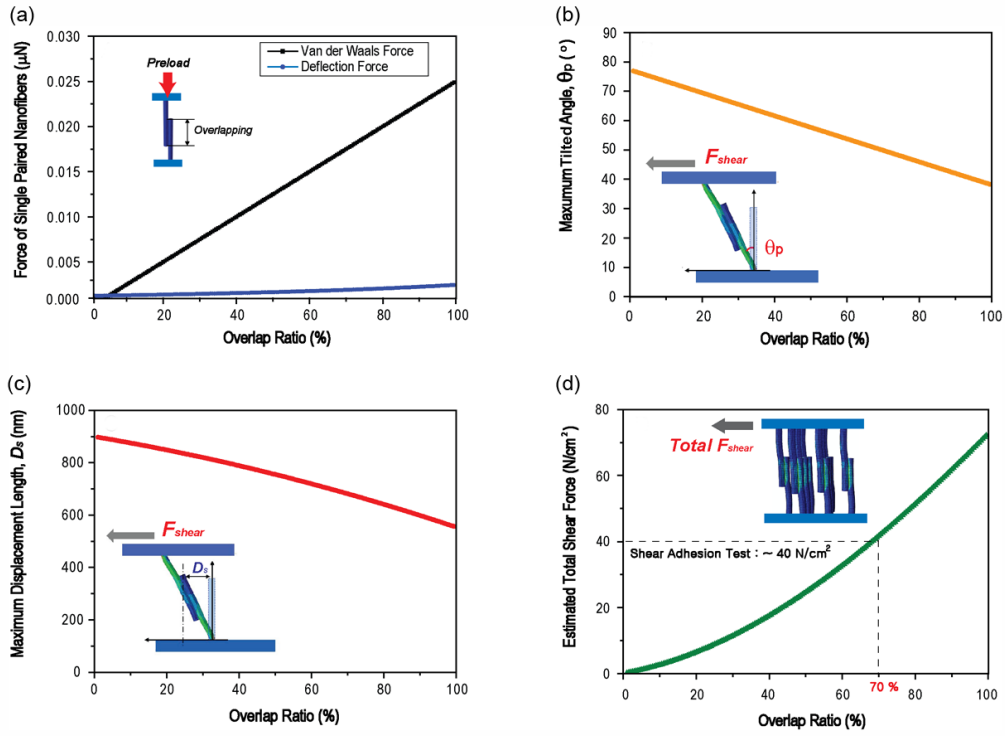


Figure 2-12. Plots of (a) F_{vdw} , F_{def} , (b) θ_p , and (c) D_s of single paired fibers and (d) F_{shear} as a function of $\alpha_{overlap}$.

2-2-4. Summary

Inspired from the wing-fixation device in beetle, we have presented the preload-dependent reversible mechanical interlocking between regularly-arrayed, high-AR polymer fiber arrays. Our experimental and theoretical studies demonstrated that the shear adhesion force is strongly affected by the applied preload (0.1~10 N/cm²); the higher the preload, the higher the shear adhesion force. From the cross-sectional SEM images of interconnected hairs, we have confirmed the increase of overlap ratio with the increase of preload, which supports the linear tendency of locking force as a function of preload. Furthermore, a simple theory was developed to explain the maximum deflection displacement/titled angle and total adhesion force, in excellent agreement with the experimental data. The current work provides an insight into how densely populated hair arrays form reversible, interconnected structures and the locking force varies with different preload in such paired structures.

Chapter 3. Beetle-inspired bi-directional, asymmetric interlocking using geometry-tunable nanohairs

3-1. Introduction

Directional, asymmetric surface architecture is an essential feature for many living organisms in nature. Examples include spider-net, [40, 41] shell of desert-beetles, [42, 43] and butterfly-wing [44] for directional water transportation, adherent gecko [45-48] and insect for active locomotion, [49, 50] and shark [51] and snake skins for low frictional surfaces. [52] These unique surface properties have been shedding light on nature-inspired smart materials and devices in a wide range of applications from water/oil repellent surfaces, contamination-free dry adhesives, to directional water harvesting. A number of reviews are available for detailed fabrication methods, mechanisms, and applications. [53-55]

In addition to the above-mentioned examples, one can observe a unique structural device in nature in the form of a reversible mechanical interlocker. A typical example is the interlocking between “hooks” and “loops” in burdock’s seeds, which is now commonly used in fabric Velcro®. Also, zoologists have observed a unique interlocking structure in insects such as dragonfly’s head arrester and beetle’s wing. [7, 37] Motivated by these observations, we recently reported that a wing-to-body locking device is present in an anterior field of the elytra as well as in an opposite field of thorax, where asymmetric microstructures called β -keratin microtrichia are reversibly interconnected to fix the wing. [56]

This directional, reversible interlocking system is potentially useful for many applications including fastener-type adhesive, [38, 56] switchable adhesion, [57, 58] electric connector, [59] biomedical patch, [60] and flexible, wet or thermal responsive adhesive. [61-63] As described shortly, regularly titled asymmetric corn-shape microhairs are observed in the wing locking device, whose functionality in reversible attachment has remained unexplored.

Following our earlier observation on reversible interlocking with vertically oriented hairs in chapter 2, [56, 64] we present here bi-directional, asymmetric interlocking between tilted, high aspect-ratio (AR) micro- and nanohairs utilizing geometry-tunable replica molding and broad ion beam irradiation. In the broad ion beam irradiation, the as-formed hairy structures are irradiated by Ar ion beam at a tilting angle ($0 \sim 90^\circ$) with an appropriate intensity and time, thereby controlling the bending angle in a precise manner. This method is advantageous over oblique e-beam irradiation as the structural transformation is completed rapidly (< 1 min) on a large area. [21, 65] Using this method, various stooped micro- and nanohair arrays (tilting angle, $\delta < 40^\circ$) were formed, and then reversibly interconnected each other to measure the shear locking force. It turned out that the maximum force was as high as ~ 60 N/cm² when the two surfaces were pulled in the reverse direction with respect to the bending angle. The hysteresis in this asymmetric, bi-directional adhesion was measured to be ~ 3 , which was in a good agreement with a simple theoretical model.

3-2. Experimental

3-2-1. Fabrication of various tilted nanohairs

The as-prepared vertical nanohairs were put into an end-Hall type linear ion gun system (Alcatel Vacuum Technology, France) to irradiate Ar gas to the nanohairs. After evacuating air, the anode voltage was kept constant at 1 keV during ion treatment with a current density of $50 \mu\text{A}/\text{cm}^2$ and a radio frequency (RF) bias voltage of -600 V was applied to the sample holder with an Ar gas flow rate of 8 sccm for the duration of 1 min. The incident angle of ion beam was varied by tilting the sample holder (40° , 55° , and 65°), resulting in various bending angles of hairs of 15, 30, and 40° . [65] For characterization and adhesion tests, six experimental sets were prepared: tilted microhairs (0 and 40°) of $1.5\text{-}\mu\text{m}$ radius, $30\text{-}\mu\text{m}$ height (PU elastomer), and tilted nanohairs (0 , 15 , 30 , and 40°) of 50-nm radius, $1\text{-}\mu\text{m}$ height (s-PUA). The SR was set at 3 for all samples.

3-2-2. Adhesion tests for bi-direction analysis

To analyze asymmetric adhesion properties, the upper and lower surfaces ($1 \times 1 \text{ cm}^2$ area each) of stooped micro- or nanohair arrays were brought into contact with a preload of $\sim 5 \text{ N}/\text{cm}^2$ and reversibly interconnected. Using a custom-built equipment (see **Figure 2-3**), a uniform pulling force was applied to

the sample with a velocity of ~ 1 mm/sec, until an adhesion failure occurred. In this way, shear adhesion forces were measured in the angled (+) and the reverse (-) directions with respect to the initial bending geometry. All measurements were repeated at least 10 times at ambient temperature under a relative humidity 50% and average values were used for the plots.

3-2-3. Detailed derivation of maximum angular displacement of hairs $\Delta \theta_p$

In order to obtain an expression for the maximum angle displacement of nanohairs before separation, we can assume the Amonton's first law of friction ($F_f = \mu F_{vdw}$). Additionally, we have to consider the force balance induced by deflection of the paired hairs ($\Delta \theta$). According to the force balance, the interlocked hairs would maintain the merged state until $F_{def} \sin \Delta \theta_p < \mu(F_{vdw} - F_{def} \cos \Delta \theta_p)$ as show in **Figure 2-2**. When the bending force is equal to or larger than the van der Waals forces, i.e., $F_{def} \sin \Delta \theta_p = \mu(F_{vdw} - F_{def} \cos \Delta \theta_p)$, the paired hairs would start to be separated. After some algebraic manipulation with Taylor-series approximation, one can have

$$\mu F_{vdw} = \Delta \theta \cdot F_{def} (\Delta \theta + \mu) \quad (17)$$

$$\Delta \theta_p \cong \frac{\mu}{2} \left[\sqrt{1 + \frac{A \cdot l \cdot (2l_0 - l)^2}{8\pi \cdot \mu \cdot E \cdot R^{3.5} \cdot D_0^{2.5}}} - 1 \right] \quad (18)$$

From equation 18, the maximum angular displacement can be derived, which is given by

$$\Delta\theta_p \cong 0.6\mu \frac{F_{vdw}}{F_{def}} \quad (19)$$

In this derivation, $F_{def} = 2EI\Delta\theta/(l_0 - l/2)^2$ assuming the condition of part-uniformly distributed load of beam deflection. [18]

3-3. Results and Discussion

Figure 3-1a shows an illustration of the actual wing locking device of beetle (*Promethis valgipes*) along with the corresponding SEM images, in which tilted microtrichia on the cuticular surface of hind wing and those on the insect body are interlocked with directionality. The SEM images demonstrate that the microhairs are of corn shape and angled with pointed directionality. When beetles fold their wings on a tree or a ground, an asymmetric interconnection is expected to occur with bi-directional high shear adhesion as schematized in **Figure 3-1b**, while a normal lift-off would be extremely simple and effortless. This wing locking device is highly reversible and does not require additional physical load or surface modification. [56] **Figure 3-1c** provides an illustration of directional, asymmetric shear force in the angled (+) and the reverse (-) directions. Here, the (+) direction denotes the direction towards the edge of beetle's torso, while the (-) direction to the center of body. From our observation, the microtrichia on the beetle's hind-wing consist of $\sim 40^\circ$ tilted micro-fibers of $\sim 2.5\text{-}\mu\text{m}$ diameter and $\sim 17\text{-}\mu\text{m}$ height (AR = ~ 8) (**Figure 3-1a**, right top image). In contrast, the slanted microstructures on the insect body are of $\sim 1.5\text{-}\mu\text{m}$ diameter and $\sim 15\text{-}\mu\text{m}$ height (AR = ~ 10) (**Figure 3-1a**, right bottom image). Both structures are regularly ordered with hexagonal packing layout with the spacing ratio (SR) of ~ 3 . Here, SR is defined as the distance between hairs divided by width.

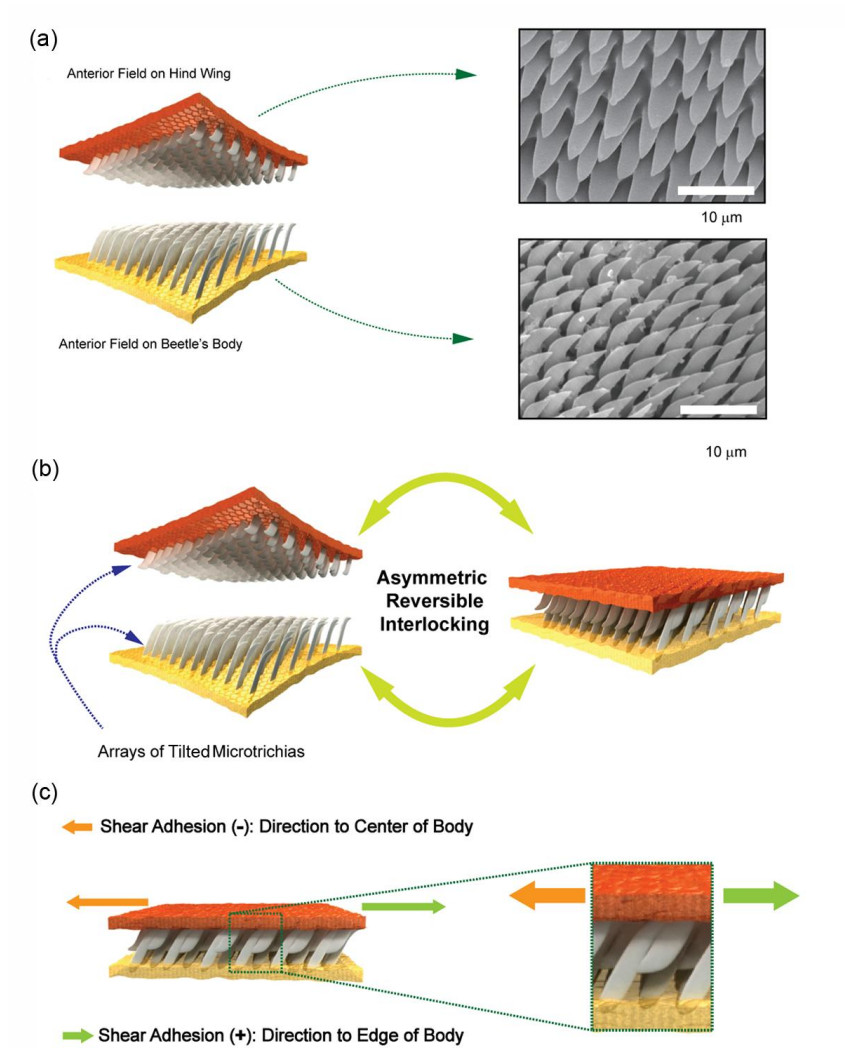


Figure 3-1. (a) Illustration of the actual wing locking device of beetle (*Promethis valgipes*) along with the corresponding SEM images, in which tilted β -keratin microtrichia on the cuticular surface of hind wing and those on the insect body are interlocked. (b) Illustration of folding and unfolding states of the wing locking device. (c) Illustration of directional, asymmetric shear force in the angled (+) and the reverse (-) directions.

To investigate directional properties of reversible interconnection, vertical and tilted microhair arrays ($\delta \sim 40^\circ$) of 1.5- μm radius and 30- μm height (SR = 3) were prepared with polyurethane elastomer (elastic modulus: 3 MPa) as shown in **Figure 3-2a-b**. As can be seen from the images, the microhairs were uniformly fabricated over a large area and nearly straight even in the stooped state. Using these microhairs, the shear adhesion force was measured by using a custom-built equipment in the angled (+) and the reverse (-) directions. By applying a uniform preload of $\sim 5 \text{ N/cm}^2$, two identical surfaces with vertical or titled hairs are brought in contact, forming a microstructural interconnection. The measurement of shear adhesion for the three cases is shown in **Figure 3-2d**. In the case of interlocking between stooped hairs, the measured shear locking forces were $\sim 9.5 \text{ N/cm}^2$ in the (+) direction and $\sim 15 \text{ N/cm}^2$ in the (-) direction, whose adhesion hysteresis is ~ 1.6 . In comparison, the force between vertical hairs was $\sim 12.5 \text{ N/cm}^2$, which lies in between the two values. Based on these results, it can be thought that the directionality of microstructures may serve for preventing the elytra from shifting along the middle of insect mass (- direction) so as to fix the delicate wings more safely during folding and unfolding states.

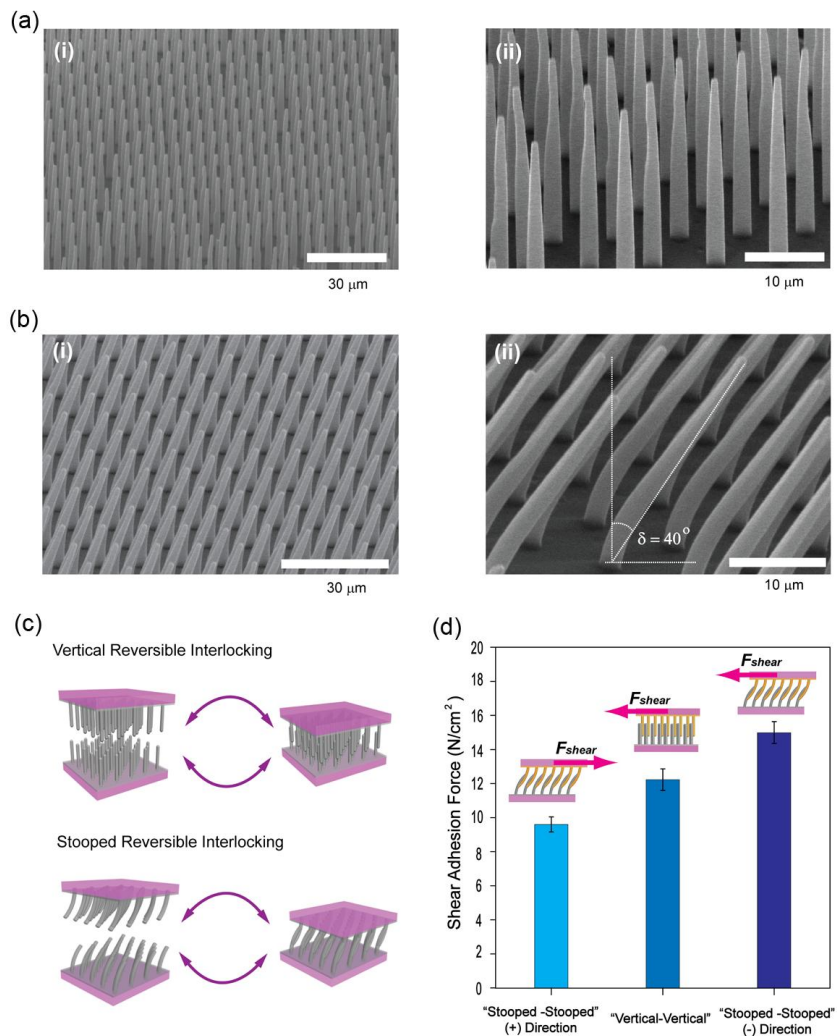


Figure 3-2. (a-b) SEM images of the as-prepared vertical PU elastomer hairs of 1.5- μm radius, 30- μm height (SR = 3) with hexagonal layout (a) and the same microfibers after oblique broad ion beam irradiation (b) Large-area (i) and magnified views (ii) are shown for each sample. (c) Illustration of reversible cycle of attachment and detachment for shear adhesion tests. (d) Measurement of shear adhesion forces for vertical and asymmetric interlocking in the (+) and (-) directions.

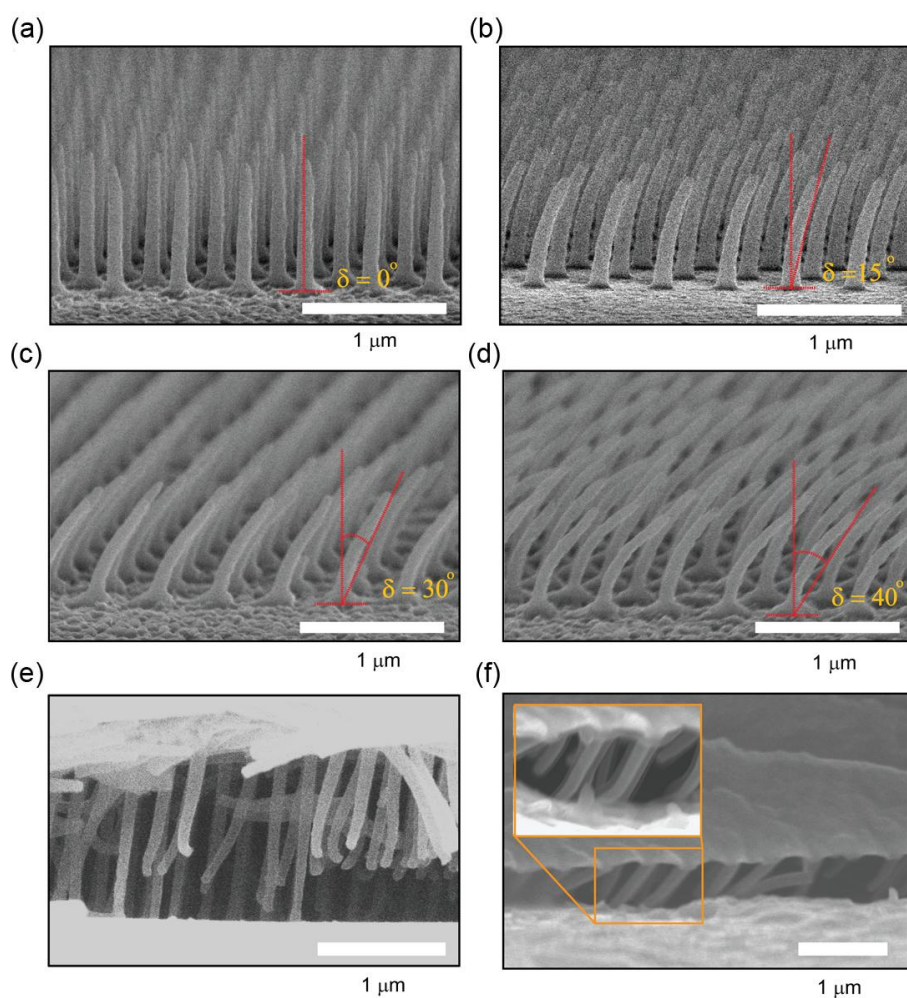


Figure 3-3. SEM images for geometry-controlled nanofiber arrays. (a) Vertical nanohair arrays. (b-d) Various tilted nanohairs by oblique broad ion beam irradiation: (b) $\delta = 15^\circ$, (c) 30° , and (d) 40° , respectively. (e, f) Cross-sectional SEM images of paired nanohairs for (e) vertical and (f) tilted nanohairs. Here, the geometry of nanohairs is the same: 50 nm radius, 1 μm height, and $\text{SR} = 3$ with hexagonal layout.

To elaborate on the effect of tilting angle in directional interlocking, we prepared various geometry-controlled nanofiber arrays of 50-nm radius and 1- μm height (SR = 3) with hexagonal layout and measured shear adhesion using soft PUA material (~ 19.8 MPa). **Figure 3-3a-d** shows polymeric nanohairs with a range of tilting angles ($\delta \sim 0, 15, 30,$ and 40°) via replica molding and oblique broad ion beam irradiation. The cross-sectional SEM images in **Figure 3-3e-f** provide an insight into how the interlocking contact is mediated by van der Waals force between vertical or titled ($\delta = 40^\circ$) nanohairy surfaces. The estimated ratio of overlapping was 60~80% between the upper and lower hairs with some broken and misaligned structures. Also, it is noted that the titled hairs are preserved during the entire bonding and pulling steps (see yellow-box in **Figure 3-3f**).

In order to understand the asymmetric interlocking behavior presented here, the step-by-step events that may occur in the course of interlocking and pulling in the angled and reversed directions are schematically drawn in **Figure 3-4**. Also, a simple theoretical model is needed to quantitatively describe the measured adhesion forces for vertical and tilted hairs. Once the hairs are brought into contact by a uniformed preload, the hairs are paired by van der Waals forces (F_{vdw}) as shown in **Figure 3-4a** (step 1), in which $F_{vdw} = A\sqrt{R} \cdot l / (16D_0^{2.5})$ [17]. Here, A is the Hamaker constant ($\sim 2.09 \times 10^{-20}$ J for polyurethane materials used in our experiment. See also supplementary information), R is the radius of nanohairs (50 nm), D_0 is the cut-off distance between hairs (0.4 nm), and l is the overlapping length, which is approximately $\sim 70\%$ of the total length of hairs as supported by the SEM images in **Figure 3-3e-f**. As illustrated in a series of steps 2-3, the

interconnected nanohairs are displaced by an applied shear load and finally separated when F_{vdw} is overwhelmed by the bending force, F_{def} . Here, F_{def} may be viewed as an disjoining force to separate two surfaces, which can be expressed as $F_{def} = 2EI\Delta\theta/(l_0 - l/2)^2$ assuming the condition of part-uniformly distributed load of beam deflection, [56] in which I is the moment of inertia ($I = \pi \cdot R^4/4$), E is the elastic modulus of the soft PUA material (~ 19.8 MPa), and l_0 is total length of hair (see **Table 2-2**).

To derive a condition for the onset of separation, we introduce here an angle displacement from the initial interlocked position ($\Delta\theta$). Consequently, the maximum angular displacement ($\Delta\theta_p$) is given from the force balance between attractive F_{vdw} and disjoining F_{def} such that $F_{def} \sin \Delta\theta_p = \mu(F_{vdw} - F_{def} \cos \Delta\theta_p)$ where μ is the frictional coefficient, ~ 0.04 . [56] After some algebraic manipulation, $\Delta\theta_p$ can be simply expressed as a ratio between F_{vdw} and F_{def} , yielding

$$\Delta\theta_p \cong 0.6\mu \frac{F_{vdw}}{F_{def}} \quad (19)$$

For the conditions used in our experiment, $\Delta\theta_p$ is approximated to 42° regardless of the pulling direction (see supplementary information for detailed derivation).

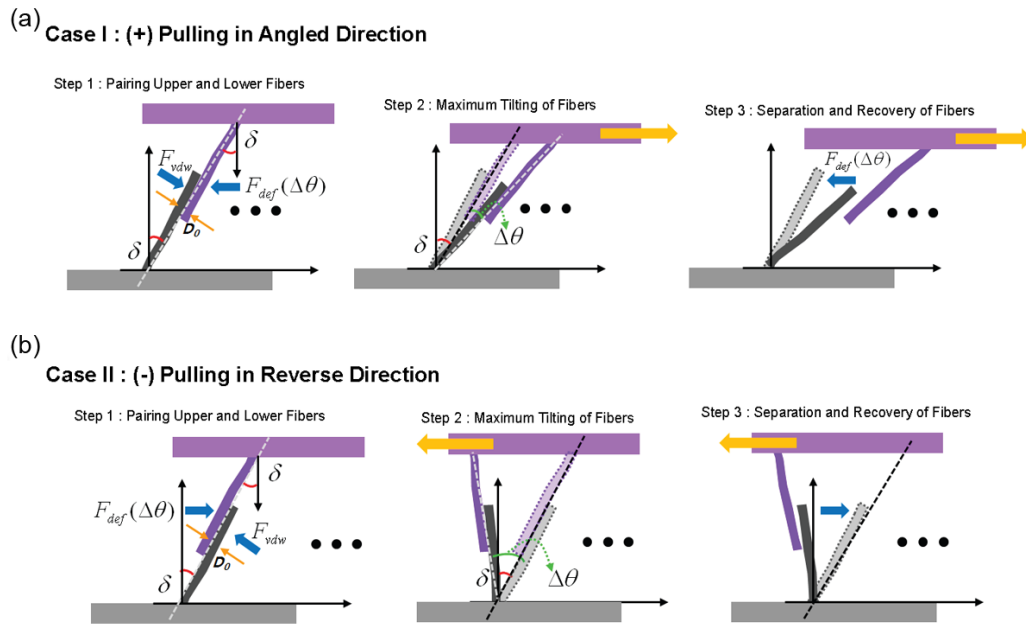


Figure 3-4. (a-b) Illustrations for step-by-step events of bi-directional, asymmetric interlocking of single paired nanofibers in the (a) angled (+) and (b) reverse (-) directions. First, the upper and lower tilted nanofibers are paired (step 1), bended to the maximum angular displacement ($\Delta \theta_p$) before separation (step 2), and finally separated by external shear force (step 3).

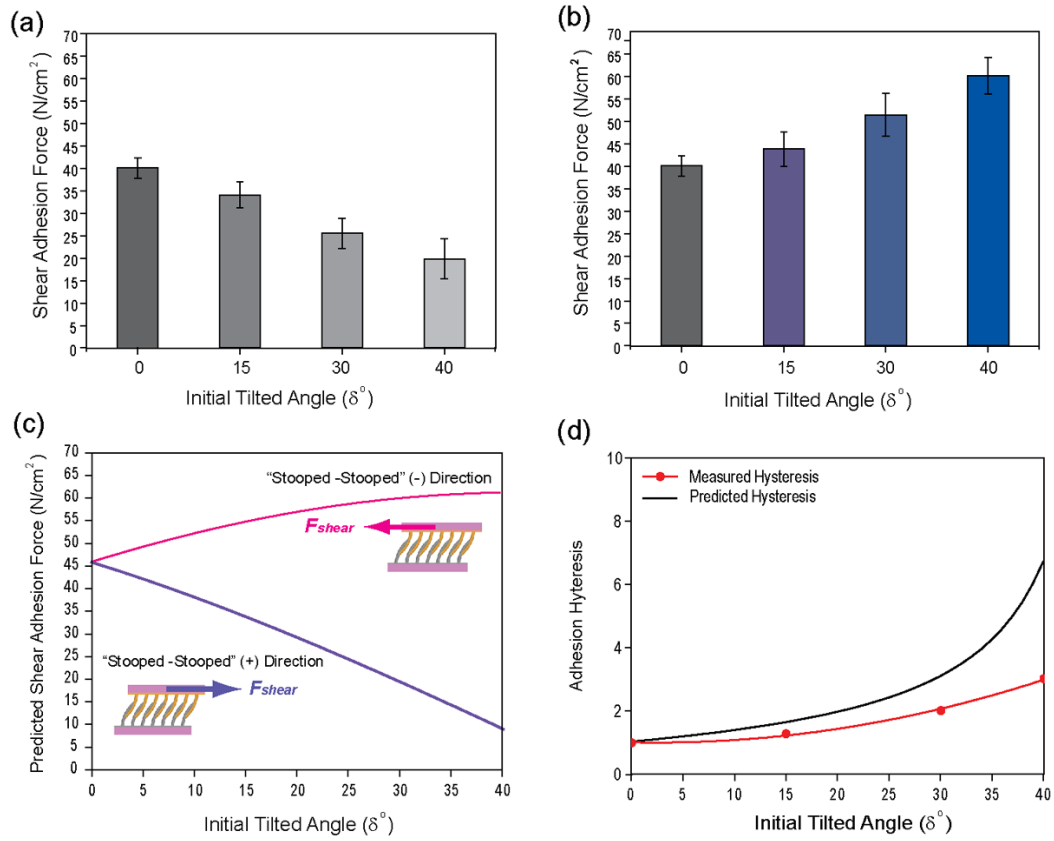


Figure 3-5. (a-b) Measurement of shear adhesion forces with various tilting angles in the (a) angled (+) and (b) reverse (-) directions. (c) Plots of theoretical shear adhesion forces as a function of δ in the angled (+) and reverse (-) directions. (d) Comparison of the measured adhesion hysteresis with the theory.

Additionally, the shear adhesion force can be estimated from the x-component of the force vector, in which the separating angle is either given by $\Delta \theta_f = \delta + \Delta \theta_p$ (+ direction) or $\Delta \theta_f = \delta - \Delta \theta_p$ (- direction) considering the geometry of tilted nanohairs. Then one can have

$$F_{shear} = \rho F_{vdw} \cos(\delta \pm \Delta \theta_p), \quad \{+ : \text{angled}\} \text{ or } \{- : \text{reverse}\} \quad (20)$$

Here, ρ is the pillar density per unit area ($\sim 18.5 \times 10^9 / \text{cm}^2$), and δ is the initial tilting angle of nanohairs. Accordingly, the hysteresis (H) is given by

$$H = \frac{\rho F_{vdw} \cos(\delta - \Delta \theta_p)}{\rho F_{vdw} \cos(\delta + \Delta \theta_p)} \quad (21)$$

Figure 3-5a-b shows the measured adhesion forces when pulled in the (+) and (-) directions, respectively, as a function of δ . In the angled direction, the measured force monotonically decreased from ~ 40 to $\sim 20 \text{ N/cm}^2$ with the increase of δ , which can be easily imagined intuitively as the hairs had been initially angled in that direction. In the reverse direction, on the other hand, the force increased from ~ 40 to $\sim 60 \text{ N/cm}^2$ with the increase of δ , which also agrees with our intuition and the theoretical model in Eq. 17. To further demonstrate this asymmetric adhesion, two pendulums (3 kg in - direction and 1 kg in + direction) were supported by $0.8 \times 0.8 \text{ cm}^2$ patches with different pulling directions (see **Figure 3-6**). Also, this asymmetric, bi-directional adhesion may be utilized as a simple, smart fastener to fix items with moderate weight when two different

pulling forces are needed in a controllable fashion as show in **Figure 3-7** with snapshots.

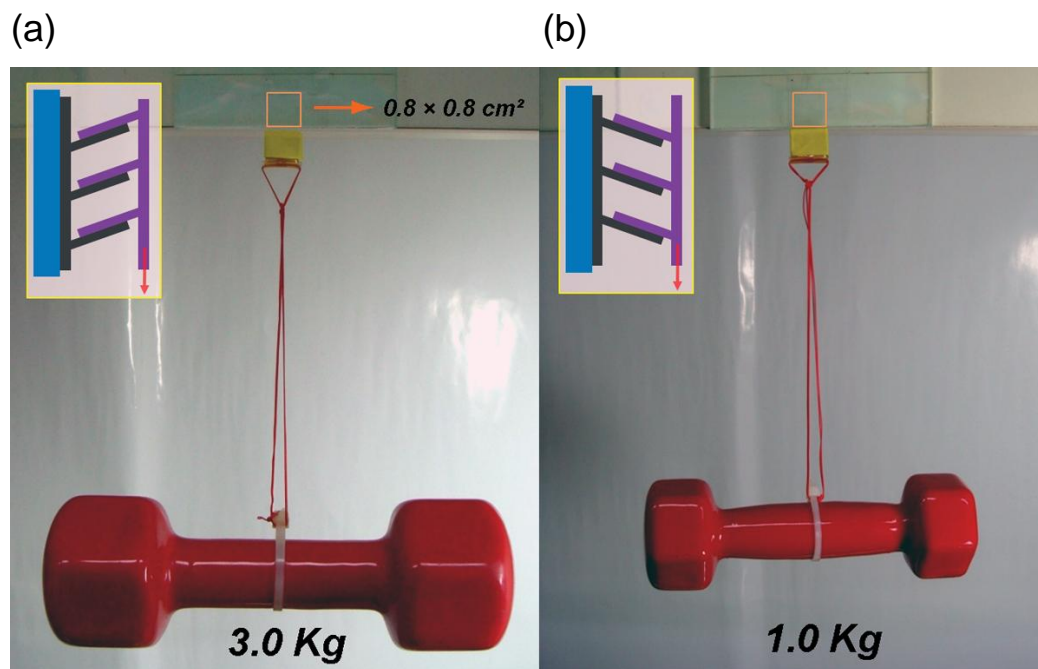


Figure 3-6. Demonstration of directional, asymmetric adhesion with two different pendulums. Two pendulums are supported by $0.8 \times 0.8 \text{ cm}^2$ patches with 3 kg for – direction (a) and 1 kg for + direction(b).



Figure 3-7. Demonstration of the utility as a simple fastener to hold a lap-top computer on a $\sim 50^\circ$ slope surface with $1 \times 1 \text{ cm}^2$ patches.

To compare with the theoretical model, the estimated shear adhesion forces are plotted as a function of δ in the (+) and (-) directions, respectively, in **Figure 3-5c**. As shown, the theoretical predictions are in good agreement with our experimental observations. Some discrepancy may be related to misalignment of upper and lower hair arrays and structural defects. In particular, the maximum hysteresis is estimated to be ~ 7 for $\delta = 40^\circ$, which is substantially higher than the measured value of ~ 3 . Since the tilted hairs are not straight, but stooped as can be seen from the SEM images in **Figure 3-3**, the actual tilting angle would be effectively lowered. For example, if we insert $\delta = 30^\circ$ in Eq. 18, the hysteresis is about 3, which is in excellent agreement with the prediction shown in **Figure 3-5d**.

3-4. Summary

We have presented bi-directional, asymmetric interlocking between tilted micro- and nanohair arrays inspired from the actual wing locking device of beetles. As expected, the measured shear force turned out to be higher in the reverse direction than that in the angled direction, suggesting that the directionality of tilted microtrichia may play a critical role in preventing the elytra from shifting along the middle of insect body. A maximum shear locking force of $\sim 60 \text{ N/cm}^2$ was observed for the nanohair arrays of 50-nm radius and 1- μm height ($\text{SR} = 3$) with a hysteresis as high as ~ 3 . A simple theoretical model was developed to describe the measured asymmetric adhesion forces and hysteresis, which were in good accordance with the experimental data.

Chapter 4. A multiplex, flexible, real-time strain gauge sensor using reversible interlocking of nanofibers

4-1. Introduction

Recently, flexible, skin-attachable or skin-like electronic sensors have been introduced based on various detection schemes, such as mechanical, chemical, thermal, and optical principles with multiscale architectures [66-75]. In general, to be able to measure spatial distributions of an input pressure, a number of circuit elements involving organic/inorganic matrix arrays [66, 69, 72-77], hybrid composites [38, 68, 78, 79], and nanowire or nanotube assemblies [67, 70, 80] need to be integrated on various flexible substrates [81]. A striking example of an integrated, multifunctional epidermal skin sensor has been demonstrated very recently by Rogers and coworkers, in which various circuit and detection components were monolithically assembled on a flexible silicon network. [66] Despite the potential and high-performance of these devices, a wearable, multiplex skin sensor still presents challenges because a large-area fabrication of the integrated device with nanomaterial assemblies (e.g., transistors, nanowires or nanotubes) would be, in many cases, complicated, expensive and minimally reproducible.

Piezoresistive sensing, which translates a mechanical displacement into an electric signal, is useful for monitoring a minute structural deformation in flexible

supporting layers over time. In this case, the difference of conductance or resistance can be measured from a specific active matrix with or without an on/off switchable transistor [66-70, 72-75]. Other interesting mechanotransduction systems can be found in nature, such as cochlear hair cells [82], intestine [83] and kidney cells [84], integrin-receptors of adhered cells [85], and endoplasmic reticulum stress, [86] all of which involve a distortion of nanocilia or biological ‘interlocking’ of hairs under a flow condition. Inspired by this hair-to-hair interlocking, as well as by the wing-locking device of beetles [87], we present a layered strain gauge sensor based on nanoscale mechanical interlocking between metal-coated, high-aspect ratio (AR) nanofibers. The mechanical sensing is enabled by numerous tiny contacts between the neighboring high-AR fibers on flexible supporting surfaces. It should be noted that two layers of regularly ordered, high-AR polymer fibers (50 nm radius and 1 μm height, AR = 10, hexagonal layout), when brought in conformal contact with each other after metal deposition, can be used as a reversible electric interlocker. Here, a shear locking force is generated by the amplified van der Waals forces of the high-density nanofibers, and a tiny distortion caused by hair-to-hair contact can be transmitted to the detector via a change in electrical resistance (piezoresistive sensing) [87].

The interlocking-based strain gauge sensor presented here can detect multiple ‘skin-like’ mechanical loadings (pressure, shear, and torsion) using metal-coated, high-AR polyurethane (PU)-based nanofibers (elastic modulus: 19.8 MPa). With the help of flexible PDMS supports and a low-noise environmental analyzer with an extremely small interval recording (100 Hz), each nanoscale deformation can be monitored in such a way that the corresponding external

stimulus is converted into a difference in the electrical resistance signal. In addition, each stimulus demonstrates a unique, discernible magnitude and pattern of the measured signal (i.e., GF) that can be used as an index to decouple three different loadings of pressure, shear, and torsion. In addition, we observed highly repeatable and reproducible signals over multiple cycle tests (<10,000 cycles) with well-defined on/off switching behaviors of loading and unloading by utilizing a pressure controller with precise piezoelectric stepping positioner and a computer-based user interface with 100 Hz recording.

4-2. Experimental

4-2-1. Fabrication and measurement of multiplex, flexible strain gauge sensors.

Two layers of 5–30 nm Pt-coated PUA nanohair arrays (maximum sample area: $9 \times 13 \text{ cm}^2$ as shown in Figure 1b) were brought into contact to make an Ohmic-like contact. Then, thin oxygen-plasma-treated PDMS supports with a thickness of $\sim 500 \mu\text{m}$ were permanently sealed to both interlocking layers to ensure stable flexibility. To analyze the electric characteristics of the sensor shown in Figures 2-4, the two PDMS-supported nanohair arrays were reversibly interlocked with an overlap area of $4 \times 5 \text{ cm}^2$. Finally, the Pt-coated terminal regions were connected with wires to make stable electrical connections. The applied strains were measured by the LK-Navigator interface via an LKG 30-KEYENCE laser displacement sensor (100 Hz interval recording) and defined by the percentage change of the substrate length. The resistance differences were recorded by the analyzing interface via two-wire resistance measurements with controllable frequency ($< 100 \text{ Hz}$, NI Digital Multimeter of NI PXI 4071 and NI PXI-1033) aided by low-leakage/low-thermal cable set. The I-V characteristics for the pressure, shear, and torsional loads were obtained by a ZAHNER® analyzer where the corresponding changes in the electrical resistance were monitored. For the analysis of detailed force responses (response time and hysteresis), a computer-based user interface and a micro force sensor (FT-S270) with nanoscale-controlled stage by piezoelectric stepping positioner (SLC-1730) were

used to apply an external pressure of ~ 550 Pa with frequency of up to 10 Hz. The applied load was gradually increased for sensing pressure (total of 8 measurements from 5 Pa to 1500 Pa), shear (total of 7 measurements from 0.001 N to 1.000 N), and torsion (total of 6 measurements from 0.0002 Nm to 0.1000 Nm). For the measurement of spatial distributions of an input pressure, an interconnected sensor network of 64 pixels with various pixel sizes from 5 to 16 mm^2 were fabricated over an area of $8 \times 5 \text{ cm}^2$ by utilizing a shadow mask deposition process.

4-3. Results and Discussion

Figures 4-1a-d show schematic illustrations for the assembly and operation of a flexible, sandwiched device in which two layers with high-density ($\sim 1.85 \times 10^9 \text{ \#/cm}^2$) nanohairs replicated from a silicon master were reversibly bonded between two flexible PDMS supports ($\sim 500 \text{ }\mu\text{m}$ thickness each). The polymer fiber arrays were replicated over a large area ($9 \times 13 \text{ cm}^2$) in a single molding step, followed by a Pt deposition process, as shown in the SEM images of **Figure 4-1c** [88, 89]. To be used in an electric application, such as in a sensor or connector, the Pt-coated nanohair arrays on the upper and lower layers were brought into contact using slight pressure ($\sim 0.1 \text{ N/cm}^2$) and then paired by the attractive van der Waals forces. As reported earlier [87, 90], the interlocking mechanism between neighboring hairs can be explained by the competition between the attractive van der Waals forces and the deflection force of the nanohairs. Specifically, the van der Waals forces between the upper and lower

hairs can be expressed as $F_{vdw} = A\sqrt{R} \cdot l / (16D^{2.5})$ [15], where A is the Hamaker constant, R is the hair radius, D is the distance between hairs, and l is the overlap length. In addition, the disjoining bending force of nanohairs is determined by the degree of deflection and material properties. It was found from our calculation [87, 90] that the van der Waals forces should be higher than the deflection force by approximately 2-3 orders of magnitude so as to generate stable electrical signals under steady conditions. When uniformly paired, a small displacement of hair-to-hair interlocking in response to an external loading can be precisely converted into a change in the electrical resistance signal with compressive deformations, as illustrated in **Figure 4-1e**.

For bending stability, both layers were permanently sealed to thin oxygen-plasma treatment PDMS supports and brought into contact to construct a sensor electric assembly [91]. As seen from **Figure 4-1b**, the assembled device shows a high degree of flexibility on the rubber-like PDMS supports. To achieve a stable electric contact, a thin layer of Pt was deposited to a thickness of 20 nm on both layers for stable Ohmic-like contact. Such a Pt deposition inevitably brings about a reduction of the shear locking force of $\sim 10 \text{ N/cm}^2$, which turned out to be sufficiently high for reversibly holding the two layers. Obviously, even without the PDMS sealing, the interlocked layers can act as an electric connector (**Figure 4-2**).

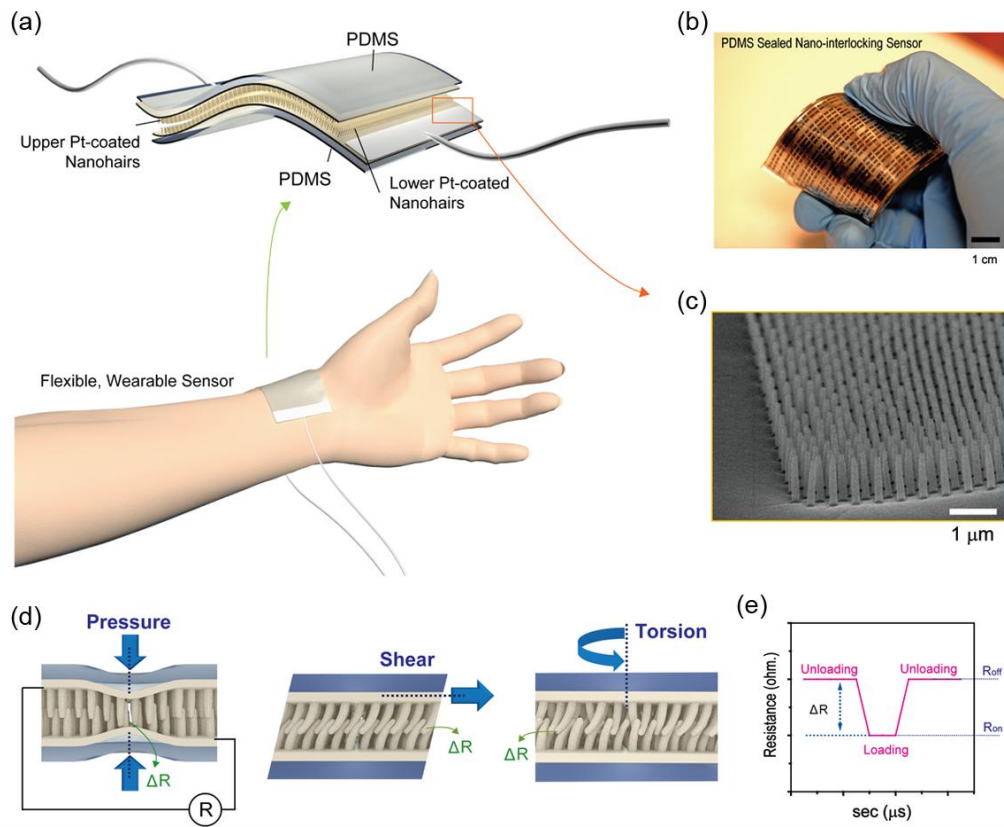


Figure 4-1. Multiplex, flexible strain gauge sensor based on the reversible interlocking of Pt-coated polymer nanofibers. (a) Schematic for the assembly and operation of a flexible sensor layer sandwiched between thin PDMS supports (~500 μm thickness each). (b) Photograph showing the flexibility of the assembled sensor. (c) SEM image of a dense array of 50-nm radius nanohairs with AR = 10. (d) Schematic illustrations of the pressure, shear, and torsion loads and their possible geometric distortions of the paired hairs. (e) Operation of a flexible sensor layer via recording of resistance change (R_{off}: unloading, R_{on}: loading).

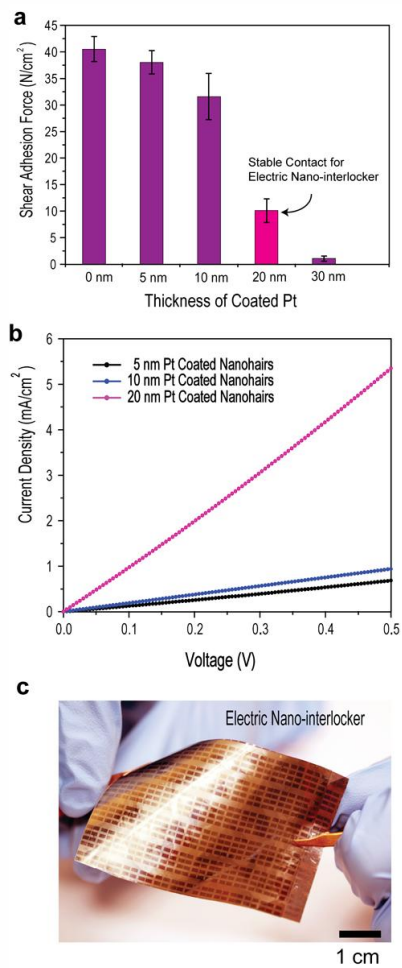


Figure 4-2. (a) Graph showing the reduction of shear adhesion force with the increase of Pt coating thickness. (b) I-V curves for various Pt-coated nano-interlockers where the 20 nm Pt-coated assembly showed a sufficiently low resistance (~ 0.6 ohm/mm) for stable Ohmic-like contact as well as a large shear adhesion force of ~ 10 N/cm². (c) Photograph of an electric connector made of Pt-coated nanofiber interlocks without PDMS sealing.

To demonstrate multiplex outputs from the mechanical stimulus, we recorded changes in the electrical resistance as a function of applied strain for three different mechanical loadings: pressure, shear, and torsion (see **Figure 4-3** for detailed experimental setup). To assess the ability of the device as a strain gauge sensor and to decouple multiple mechanical inputs, the GF of the assembled device was measured with a gradual increase of the strain up to $\leq 2\%$ (pressure), $\leq 4\%$ (shear), and $\leq 5\%$ (torsion). The measured resistance difference ($\Delta R = R_{off} - R_{on}$) and ratio ($\Delta R / R_{off}$) were plotted as a function of applied strain (**Figure 4-4a-h**), the slope of which yields the corresponding piezoresistive GF, defined as $GF = (\Delta R / R) / \varepsilon$: ~ 11.45 for pressure, ~ 0.75 for shear, and ~ 8.53 for torsion. Here, $\Delta R / R$ and ε denote the relative resistance change and applied strain, respectively. Notably, the measured GFs of pressure (~ 11.45) and torsion (~ 8.53) were significantly higher than those of the recently reported graphene-based film ($GF = 6.1$) [92] and conventional metal-alloys ($GF = 2.0$) [93].

Once interconnected, a tiny displacement between the hairs can be interpreted into a scalar change of electrical resistance, which seems analogous to chemical and biological signaling in cochlea hair cells [82] and cell-to-cell mechanotransduction [94, 95]. The displacement in individual hair-to-hair contacts was verified under each different stimulus (**Figure 4-4c, f and i**), revealing that the paired hairs are distorted in response to different mechanical loads. Using the sensor assembly, the I-V characteristics were recorded for three different mechanical loadings (see **Figure 4-5** for detailed plots), as schematically illustrated in **Figure 4-1d**. The results indicate that the three physical inputs can

be distinguished with the help of the specific GFs, which is similar to the sensory system found in the human skin [96]. Here, a small normal pressure, shear, or torsion causes an additional contact in the geometric layout of polymer hairs, which in turn produces a decrease of the contact resistance in the I-V curve (see **Figure 4-1d** and **Figure 4-5**).

For the pressure sensing, the minimum detectable pressure was as small as ~5 Pa, which is equivalent to the weight of 5 mg per 10 mm² and much smaller than a pressure induced by a gentle touch (<10 kPa) [97]. Here, the noise level was independently analyzed for a wide range of pressures (≤ 1000 Pa), suggesting that the noise signals are unavoidable but clearly distinguishable even for a small input signal down to ~5 Pa. In the case of the shear sensor, a shear load also gives rise to an additional contact among neighboring hairs, and the contact resistance decreases accordingly. The minimum detectable shear force was ~0.001 N, with the tested sensing limit being approximately 1 N (three orders of magnitude difference). In a similar manner, the torsion sensing was performed, detecting a torsional load as small as 0.0002 N·m. The multiplex sensing platform presented here, which benefits from the flexible nature of the interlocked device, is intrinsically different from previous layered sensors [66-69] in which the device was used to measure a single signal (pressure-only) or multiple signals with multiple active modules. In contrast to the pressure and torsion sensing, the GF of the shear was significantly smaller, which appears to be attributable to the relatively small increment in the number of fiber-to-fiber contacts made in response to an applied compressive strain.

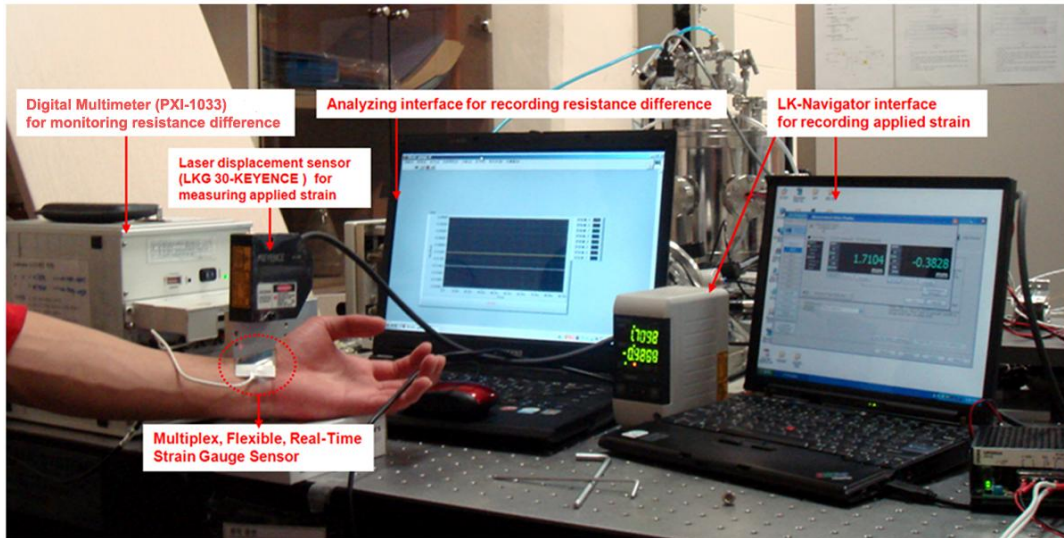


Figure 4-3. Photograph showing the detailed detection setup with a computer-based user interface via an NI Digital Multimeter (PXI-1033) for measuring the resistance differences, and a LK-Navigator interface via a LKG 30-KEYENCE laser displacement sensor for recording the applied strains.

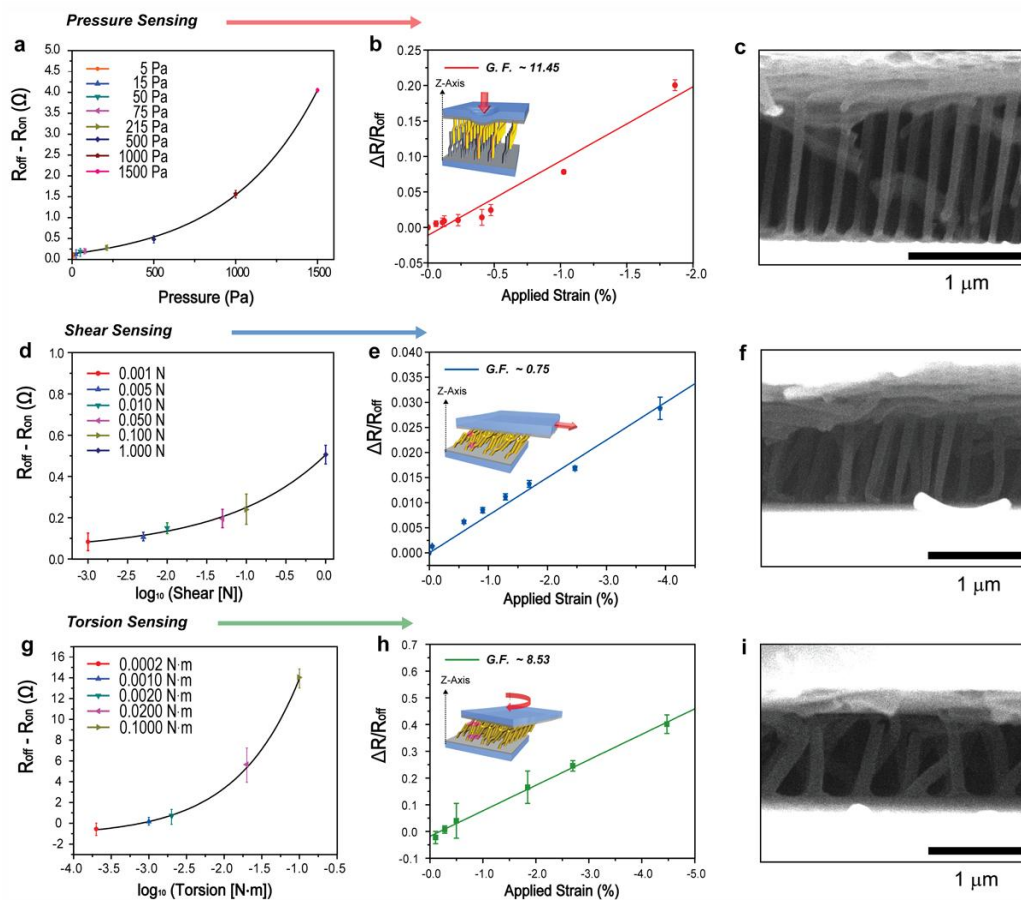


Figure 4-4. Electric characterizations of the sensor in response to pressure, shear, and torsion loads. Plots showing the difference of the electrical resistance ($R_{\text{off}} - R_{\text{on}}$) for three different mechanical loads of pressure (a), shear (d), and torsion (g) along with changes in the electrical resistance ratio as a function of applied strain for pressure (b), shear (e), and torsion (h). The corresponding SEM images on the right panel (c, f, and i) show structural displacement as a result of each physical load. The GFs were measured from the slope of each plot: ~ 11.45 (pressure), ~ 0.75 (shear), and ~ 8.53 (torsion). The error bars represent the standard deviations.

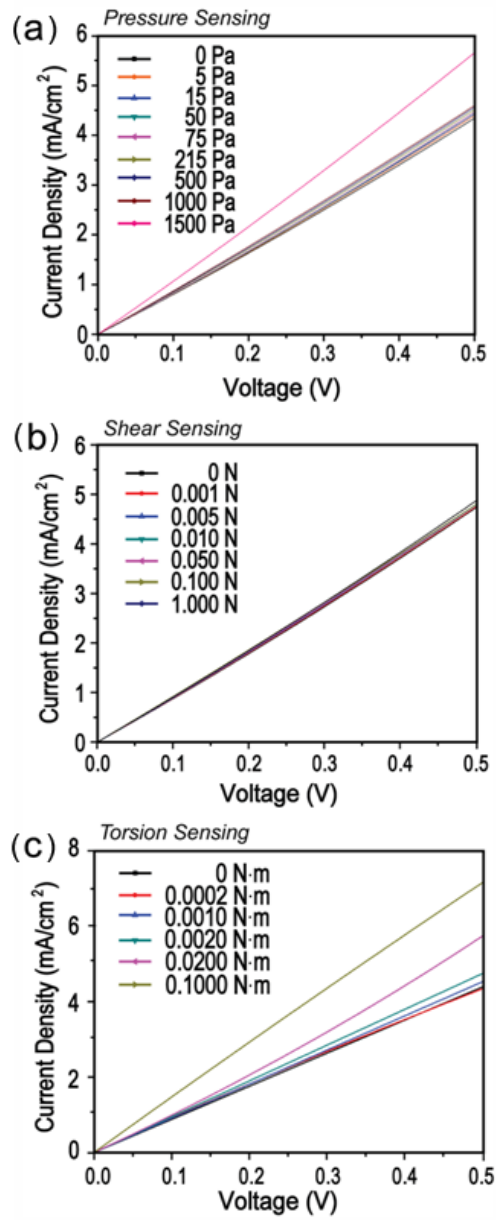


Figure 4-5. (a-c) Plots showing the detailed I-V curves for three different mechanical loadings: pressure (a), shear, (b) and torsion (c).

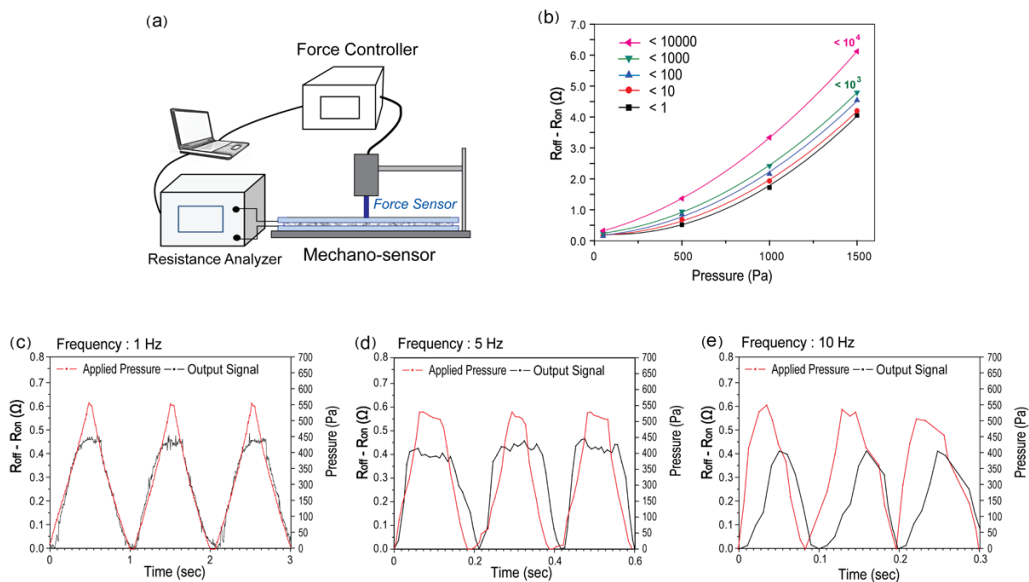


Figure 4-6. Measurement of highly sensitive, multiplex, and real-time signals (a) Schematic illustration of the measurement set-up. (b) Multiple-cycle tests ($<10,000$ cycles) with repeating loading-unloading of pressure in the range of 0 ~ 1500 Pa. (c-e) Frequency responses to various input signals as a function of time (pressure input frequency: 1 Hz): 1Hz (c), 5 Hz (d), and 10 Hz (e).

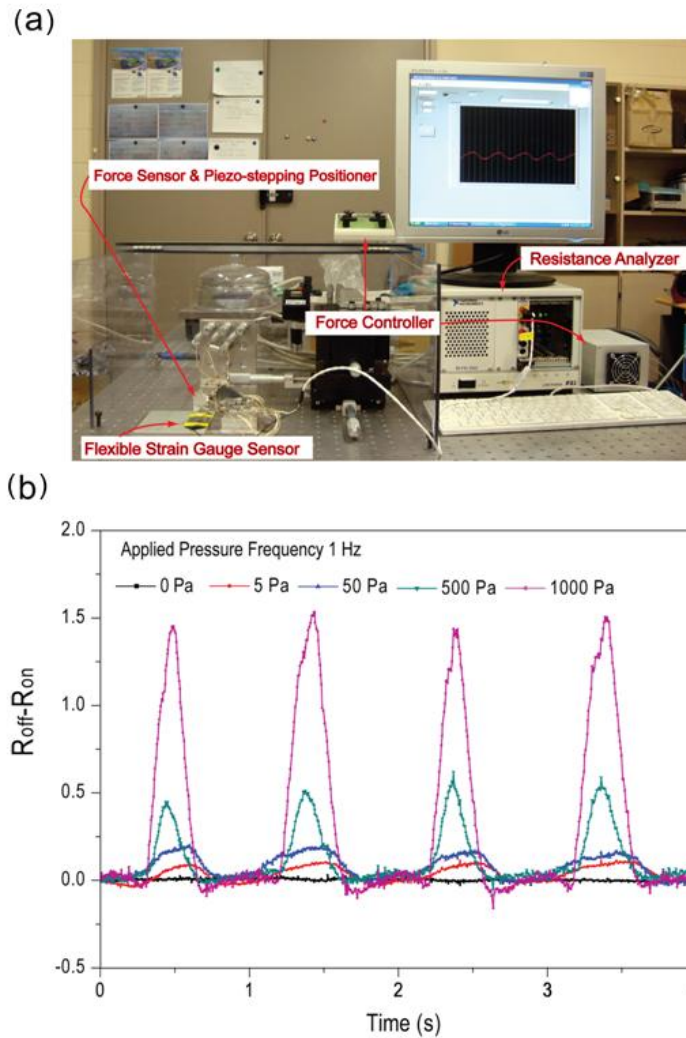


Figure 4-7. (a) Photograph of the resistance sensing set-up, which consists of a force controller, a piezoelectric strain gauge sensor, and a computer-based resistance analyzing interface with 100 Hz recording. (b) Plots of $R_{off} - R_{on}$ as a function of time (pressure input frequency: 1 Hz) for various applied pressures (0~1000 Pa). As shown, the noise level was distinguishable even for a minimum detectable pressure of ~5 Pa.

Next, we investigated multiple cycle tests (<10,000 cycles) by repeating loading and unloading of pressure (<1500 Pa) and frequency responses to various input signals with a sophisticated force controller aided by a computer-based user interface (see **Figure 4-6a** and **Figure 4-7**). As shown in **Figure 4-6b**, the output signals were stable for many thousand cycles (maximum ~8,000 cycles) without notable degradations. After approximately 10,000 cycles, the signals were shifted to higher resistance changes, presumably due to the formation of permanent and irreversible hair contacts. These observations suggest that the measurement was highly reproducible and repeatable with the same amount of mechanical loads, even after thousands of cycles.

Regarding the frequency responses (**Figures 4-6c-e**), the output signals were rapidly detectable and deterministic with minimal delay times for various frequencies (1, 5, and 10 Hz). The transformation into a trapezoidal-type response along with a slight delay for a relatively high frequency of 10 Hz may be associated with the viscoelastic response of the PDMS supports. Based on these observations, the sensor response could be reliable up to ≤ 10 Hz in terms of bandwidth. In addition, the hysteresis was measured with 1 Hz force frequency in the course of loading and unloading the pressure up to ~550 Pa (**Figure 4-8a**). This hysteresis may be attributed to elastic rearrangement of metal-coated nanofibers during unloading and viscoelastic effects of PDMS shielding layers. An additional time-resolved scan of the applied pressure and output signal shown in **Figure 4-8b** indicates that a delay time is less than < 0.05 s for an abrupt step input from 0 to 1500 Pa, in accordance with the previous response delay shown in **Figure 4-6c-e**. It is noted in this regard that the detection equipment has a very

small interval of 100 Hz (= 100 measurements per second), so that a certain physical input, regardless of the duration time, could be discriminated as a normal, shear, or torsional load.

The reversible and restorable sensing characteristic presented here is associated with the elastic ‘self-reconstruction’ of the nanofibers after release of the displacement during multiple loading-unloading cycles. In particular, the displacement from pressure, shear, and torsion, despite each input having a different direction and tortuosity, may be interpreted as an average normal strain (bending) along the z-axis in terms of a relative displacement that obeys Hook’s law [98] (see the inset schematic of **Figure 4-4**). Because a compressive strain is applied to the interconnected layers, the overlap length of nanofibers would be elevated, which in turn results in a decrease in the electrical resistance.

To elaborate on the ability to sense a tiny displacement of hairs in real time, the continuous kinetic forces of a bouncing water droplet (20 μ l) were measured by a low-noise environmental analyzer. The superhydrophobic surface with a static contact angle of $\sim 160^\circ$ and a hysteresis of $\sim 3^\circ$ was prepared following the procedure reported earlier [99]. The data were collected from the analyzer (100 Hz interval recording) while a droplet was bouncing back and forth approximately 8 times from the initial height of 5 cm for ~ 0.4 sec (**Figures 4-9a-c**). As shown, the first impact of the droplet was recorded as ~ 190 Pa, which is equivalent to $\sim \Delta 0.3$ ohm with some fluctuation in the signal due to the viscoelastic property of the PDMS substrates. Interestingly, the measured forces were highly correlated with the kinetic motion of the droplet as seen from the high-speed snapshots.

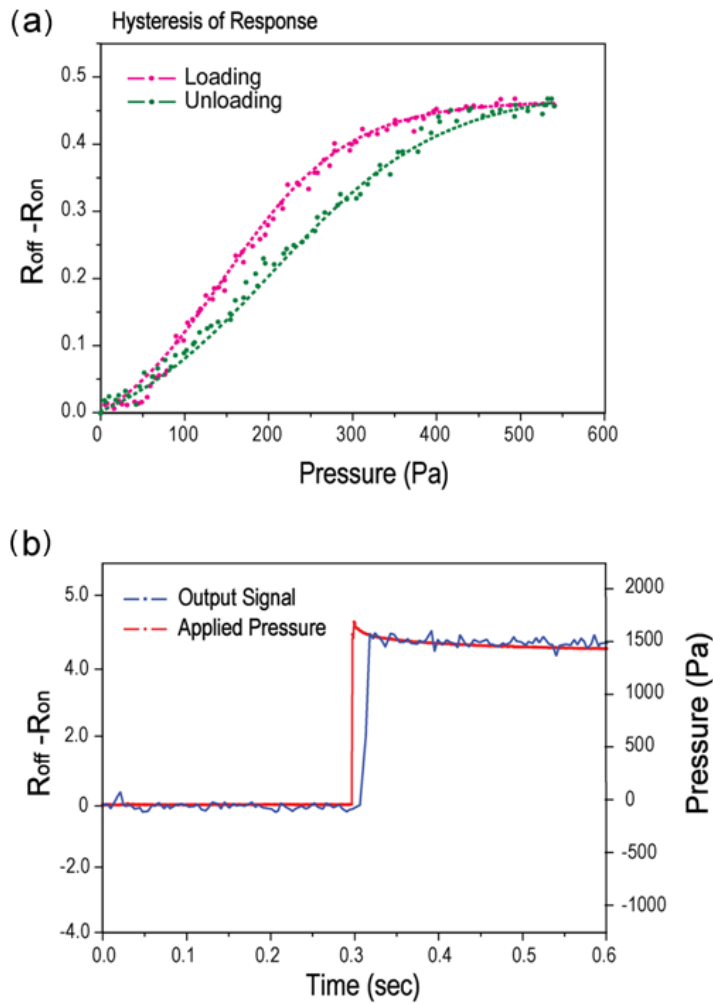


Figure 4-8. (a) Hysteresis of output electric signal for an input pressure of ~550 Pa with 1 Hz force frequency. (b) Comparison of input pressure and output signal for an abrupt step input from 0 to 1500 Pa, showing a response lag time of < 0.05 s.

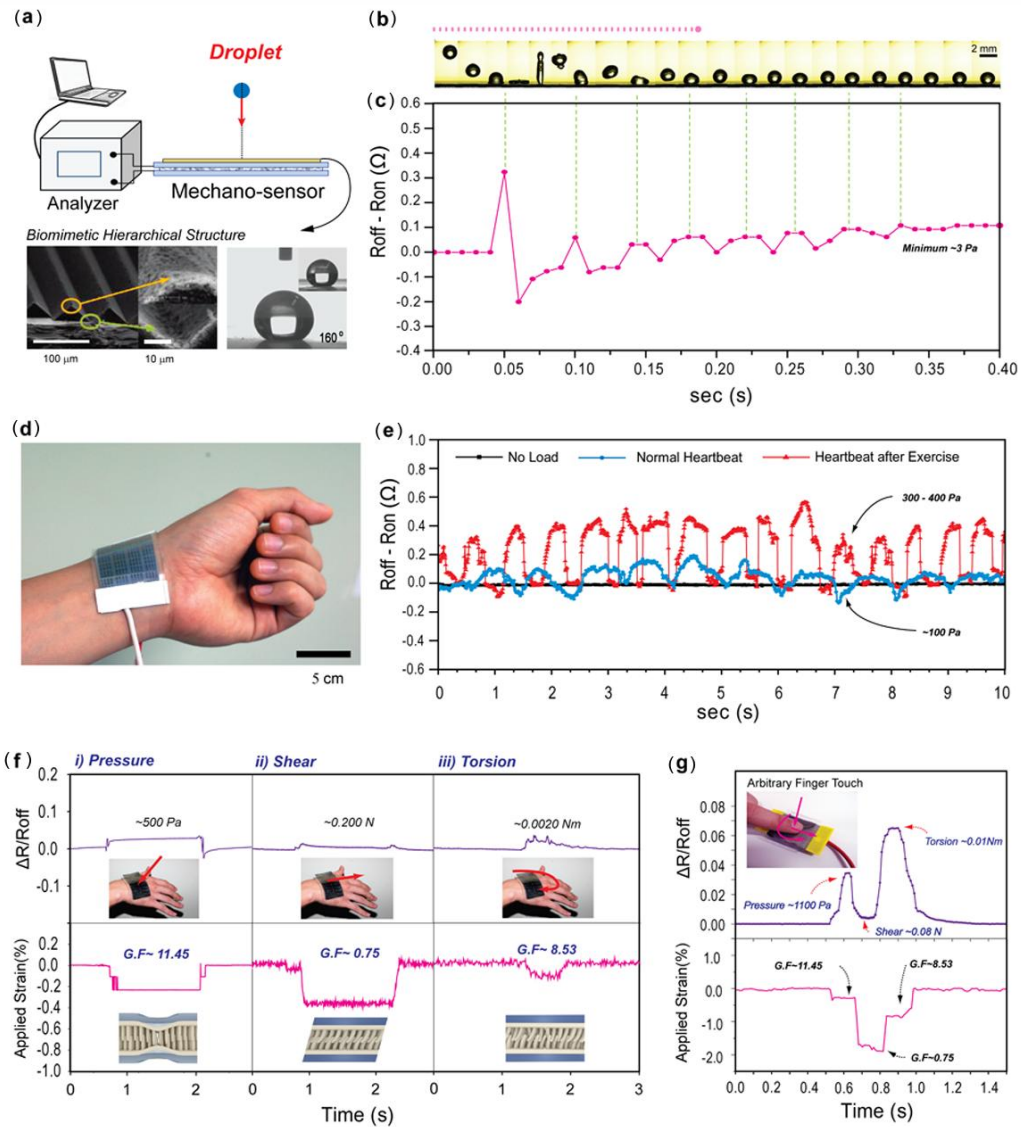


Figure 4-9. Fabrication of a sensor network to measure spatial distributions of an input pressure. (a) The schematic of a real-time, high-sensitivity measurement of the dynamic motion of a bouncing water droplet (20 μl) ~5 cm above from a

superhydrophobic surface. (Reproduced for the inset SEM image [ref. [99]]) (b) The corresponding snapshots from a high-speed camera are shown. (c) The difference in the electrical resistance ($R_{\text{off}} - R_{\text{on}}$) for the duration of ~ 0.4 sec. (d) Photograph showing the skin-attachable sensor right above the artery of the wrist. (e) Measurement of the physical force of a heartbeat under normal (~ 60 beats per min with an average intensity of ~ 100 Pa) and exercise conditions (~ 100 beats per min with an average intensity of $300\sim 400$ Pa). (f) Plots showing the detection and decoupling of pressure, shear, and torsion loads with each time-dependent signal pattern of resistance ratio and applied compressive strain as a function of time. (g) Example for the decoupling of an arbitrary finger touch with pressure, shear, and torsion.

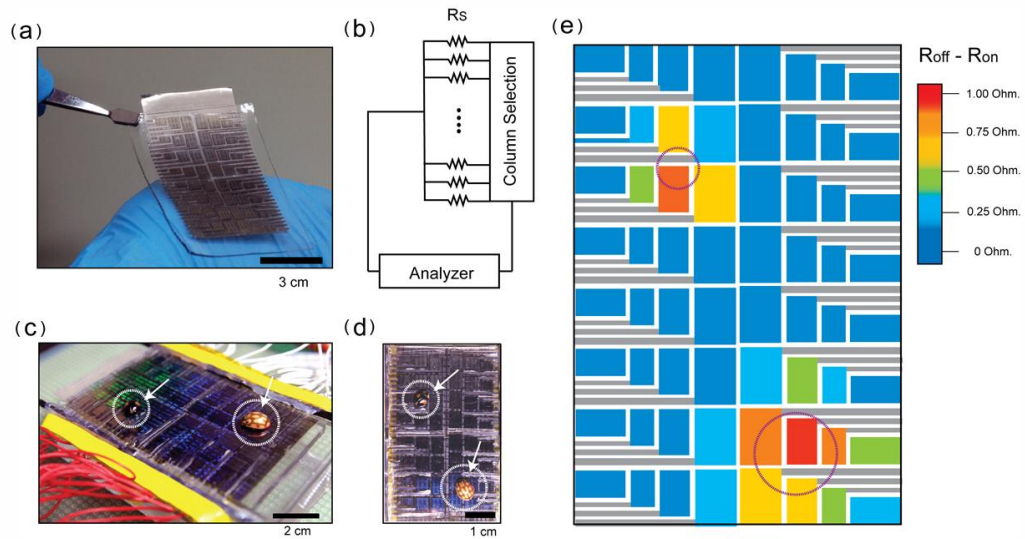


Figure 4-10. Fabrication of a sensor network to measure spatial distributions of an input pressure. (a) Photograph of a fabricated sensor network of 64 pixels over an area of $8 \times 5 \text{ cm}^2$. (b) Schematic of a circuit design. (c-d) Images of device with two lady beetles placed on two locations for pressure sensing: tilted (c) and top views (d), respectively. (e) The resulting two-dimensional intensity profile measured by mapping of the pixel signals.

In addition, the physical force of a heartbeat was monitored in real time after attaching the sensor right on the artery of the wrist. It should be noted that the flexibility of the sensor was high enough to make a conformal seal with the aid of medical tape. As shown in **Figures 4-9d-e**, under two different conditions a normal heartbeat (~60 beats per min with an average intensity of ~100 Pa) and that after an exercise (~100 beats per min with an average intensity of 300~400 Pa) were monitored with time, suggesting that the signals could be differentiated by discernible magnitudes and frequencies of the corresponding biofeedback (heartbeat). **Figure 4-9f** shows the skin-like, simultaneous detection of pressure, shear, and torsion (see inset photographs of **Figure 4-9f**) classified with each magnitude and pattern of the measured signal. Furthermore, an arbitrary signal like finger touch was analyzed into a mixed signal of the three different physical inputs on the time-dependent domain in **Figure 4-9g**. Here, both the resistance ratio and the applied compressive strain were recorded as a function of time at a 100 Hz interval.

In order to demonstrate the potential for measuring spatial distributions of the pressure, an interconnected sensor network of 64 pixels with various pixel sizes from 5 to 16 mm² were fabricated over an area of 8 x 5 cm² (**Figures 4-10a-d**). Then, two lady beetles were placed on two different locations of the device and the resulting two-dimensional intensity profiles are displayed in **Figures 4-10e**. As shown, the interconnected sensor can detect the spatial distribution of the pressure after mapping the intensity profiles. With further optimization, this flexible sensor network has the potential to be used as a skin-like, wearable health-monitoring device and further as an implantable device and prosthetic skin

partly due to its excellent flexibility and the biocompatibility of the PDMS supports.

4-4. Summary

We have presented a highly flexible, multiplex, real-time sensor based on reversible mechanical interlockers between Pt-coated, high-AR nanofibers. Our experimental results demonstrated that the GFs were ~ 11.5 (pressure), ~ 0.75 (shear), and ~ 8.53 (torsion) with a strain range of $\leq 5\%$, which are fairly comparable or superior to those of the existing graphene-based films and metal alloys. In addition, the shear adhesion force was maintained at $\sim 10 \text{ N/cm}^2$, even with a Pt coating, owing to the amplified van der Waals forces among the paired high-density nanofibers. In contrast to other detection systems, the current nano-interlocking mechanism does not involve any complex integrated nanomaterial assemblies or layered arrays, allowing for a simple, cheap, yet robust sensing platform for high-performance, large-area strain gauge sensors. Using the assembled strain sensor, we measured three different mechanical loads in the form of normal pressure, shear, and torsion with high sensitivity and wide dynamic range. In addition, the output signals were highly repeatable and reproducible over multiple cycle tests (< 10000 cycles) with excellent on/off switching behaviors. For potential applications, the assembled device was used to detect the dynamic motion of a small bouncing water droplet and the physical force of a heartbeat, shedding light on its potential use in real-time monitoring, skin-like wearable electronics or implantable medical devices.

References

- [1] A. del Campo, L. F. Boesel, C. Greiner, and E. Arzt, "Gecko-Inspired Surfaces: A Path to Strong and Reversible Dry Adhesives," *Advanced Materials*, vol. 22, pp. 2125-2137, May 18 2010.
- [2] E. Arzt, G. Huber, H. Mantz, R. Spolenak, K. Mecke, K. Jacobs, and S. N. Gorb, "Evidence for capillarity contributions to gecko adhesion from single spatula nanomechanical measurements," *Proceedings of the National Academy of Sciences of the United States of America*, vol. 102, pp. 16293-16296, Nov 8 2005.
- [3] L. Jiang, H. Bai, X. L. Tian, Y. M. Zheng, J. Ju, and Y. Zhao, "Direction Controlled Driving of Tiny Water Drops on Bioinspired Artificial Spider Silks," *Advanced Materials*, vol. 22, pp. 5521-5525, Dec 21 2010.
- [4] M. Sitti, "MINIATURE DEVICES Voyage of the microrobots," *Nature*, vol. 458, pp. 1121-1122, Apr 30 2009.
- [5] J. A. Rogers, H. C. Ko, M. P. Stoykovich, J. Z. Song, V. Malyarchuk, W. M. Choi, C. J. Yu, J. B. Geddes, J. L. Xiao, S. D. Wang, and Y. G. Huang, "A hemispherical electronic eye camera based on compressible silicon optoelectronics," *Nature*, vol. 454, pp. 748-753, Aug 7 2008.
- [6] G. Mestral, "Separable fastening device, US patent," US patent Patent No. 3,009,235 1961.
- [7] S. N. Gorb, "Frictional surfaces of the elytra-to-body arresting mechanism in tenebrionid beetles (Coleoptera : Tenebrionidae): Design of co-opted fields of microtrichia and cuticle ultrastructure," *International Journal of Insect Morphology & Embryology*, vol. 27, pp. 205-225, Jul 1998.
- [8] R. S. Fearing, H. Ko, J. Lee, B. E. Schubert, Y. L. Chueh, P. W. Leu, and A. Javey, "Hybrid Core-Shell Nanowire Forests as Self-Selective Chemical Connectors," *Nano Letters*, vol. 9, pp. 2054-2058, May 2009.
- [9] Y. Zhao, T. Tong, L. Delzeit, A. Kashani, M. Meyyappan, and A. Majumdar, "Interfacial energy and strength of multiwalled-carbon-

- nanotube-based dry adhesive," *Journal of Vacuum Science & Technology B*, vol. 24, pp. 331-335, Jan-Feb 2006.
- [10] S. J. Choi, P. J. Yoo, S. J. Baek, T. W. Kim, and H. H. Lee, "An ultraviolet-curable mold for sub-100-nm lithography," *Journal of the American Chemical Society*, vol. 126, pp. 7744-7745, Jun 30 2004.
- [11] P. J. Yoo, S. J. Choi, J. H. Kim, D. Suh, S. J. Baek, T. W. Kim, and H. H. Lee, "Unconventional patterning with a modulus-tunable mold: From imprinting to microcontact printing," *Chemistry of Materials*, vol. 16, pp. 5000-5005, Nov 30 2004.
- [12] J. N. Israelachvili, *Intermolecular and surface forces* 2nd ed. San Diego: Academic press, 1991.
- [13] E. Ortyl, S. Kucharski, and T. Gotszalk, "Refractive index modulation in the polyurethane films containing diazo sulfonamide chromophores," *Thin Solid Films*, vol. 479, pp. 288-296, May 23 2005.
- [14] D. Tahk, T. I. Kim, H. Yoon, M. Choi, K. Shin, and K. Y. Suh, "Fabrication of Antireflection and Antifogging Polymer Sheet by Partial Photo polymerization and Dry Etching," *Langmuir*, vol. 26, pp. 2240-2243, Feb 16 2010.
- [15] D. Leckband and J. Israelachvili, "Intermolecular forces in biology," *Quarterly Reviews of Biophysics*, vol. 34, pp. 105-267, May 2001.
- [16] M. Urbakh, J. Klafter, D. Gourdon, and J. Israelachvili, "The nonlinear nature of friction," *Nature*, vol. 430, pp. 525-528, Jul 29 2004.
- [17] J. N. Israelachvili, *Intermolecular and Surface Forces: Revised Third Edition*: Academic press, 2011.
- [18] S. H. Crandall, *An Introduction to the Mechanics of Solids*: McGraw-Hill, 1999.
- [19] M. Srinivasarao, "Nano-optics in the biological world: Beetles, butterflies, birds, and moths," *Chemical Reviews*, vol. 99, pp. 1935-1961, Jul 1999.
- [20] K. Autumn and A. M. Peattie, "Mechanisms of adhesion in geckos," *Integrative and Comparative Biology*, vol. 42, pp. 1081-1090, Dec 2002.
- [21] T. I. Kim, H. E. Jeong, K. Y. Suh, and H. H. Lee, "Stooped Nanohairs:

- Geometry-Controllable, Unidirectional, Reversible, and Robust Gecko-like Dry Adhesive," *Advanced Materials*, vol. 21, pp. 2276-+, Jun 12 2009.
- [22] www.torstamp.com/Brochures/BR-122.pdf.
- [23] A. Lafuma and D. Quere, "Superhydrophobic states," *Nature Materials*, vol. 2, pp. 457-460, Jul 2003.
- [24] A. Tuteja, W. Choi, J. M. Mabry, G. H. McKinley, and R. E. Cohen, "Robust omniphobic surfaces," *Proceedings of the National Academy of Sciences of the United States of America*, vol. 105, pp. 18200-18205, Nov 25 2008.
- [25] Y. Rahmawan, M. W. Moon, K. S. Kim, K. R. Lee, and K. Y. Suh, "Wrinkled, Dual-Scale Structures of Diamond-Like Carbon (DLC) for Superhydrophobicity," *Langmuir*, vol. 26, pp. 484-491, Jan 5 2010.
- [26] Y. M. Zheng, H. Bai, Z. B. Huang, X. L. Tian, F. Q. Nie, Y. Zhao, J. Zhai, and L. Jiang, "Directional water collection on wetted spider silk," *Nature*, vol. 463, pp. 640-643, Feb 4 2010.
- [27] G. Huber, H. Mantz, R. Spolenak, K. Mecke, K. Jacobs, S. N. Gorb, and E. Arzt, "Evidence for capillarity contributions to gecko adhesion from single spatula nanomechanical measurements," *Proceedings of the National Academy of Sciences of the United States of America*, vol. 102, pp. 16293-16296, Nov 8 2005.
- [28] L. F. Boesel, C. Greiner, E. Arzt, and A. del Campo, "Gecko-Inspired Surfaces: A Path to Strong and Reversible Dry Adhesives," *Advanced Materials*, vol. 22, pp. 2125-2137, May 18 2010.
- [29] M. K. Kwak, C. Pang, H.-E. Jeong, H.-N. Kim, H. Yoon, H.-S. Jung, and K.-Y. Suh, "Towards the Next Level of Bioinspired Dry Adhesives: New Designs and Applications," 2011. *Advanced Functional Materials* vol. 21, pp. 3606- 3616 2011.
- [30] D. Chandra and S. Yang, "Stability of High-Aspect-Ratio Micropillar Arrays against Adhesive and Capillary Forces," *Accounts of Chemical Research*, vol. 43, pp. 1080-1091, Aug 2010.
- [31] M. P. Murphy, S. Kim, and M. Sitti, "Enhanced Adhesion by Gecko-

- Inspired Hierarchical Fibrillar Adhesives," *Acs Applied Materials & Interfaces*, vol. 1, pp. 849-855, Apr 2009.
- [32] H. Kim, J. Ge, J. Kim, S. Choi, H. Lee, H. Lee, W. Park, Y. Yin, and S. Kwon, "Structural colour printing using a magnetically tunable and lithographically fixable photonic crystal," *Nature Photonics*, vol. 3, pp. 534-540, Sep 2009.
- [33] S. Kinoshita and S. Yoshioka, "Structural colors in nature: The role of regularity and irregularity in the structure," *Chemphyschem*, vol. 6, pp. 1442-1459, Aug 12 2005.
- [34] A. Mahdavi, L. Ferreira, C. Sundback, J. W. Nichol, E. P. Chan, D. J. D. Carter, C. J. Bettinger, S. Patanavanich, L. Chignozha, E. Ben-Joseph, A. Galakatos, H. Pryor, I. Pomerantseva, P. T. Masiakos, W. Faquin, A. Zumbuehl, S. Hong, J. Borenstein, J. Vacanti, J. M. Karp, and R. Langer, "A biodegradable and biocompatible gecko-inspired tissue adhesive," *Proceedings of the National Academy of Sciences of the United States of America*, vol. 105, pp. 2307-2312, Feb 19 2008.
- [35] M. K. Kwak, H.-E. Jeong, and K. Y. Suh, "Rational Design and Enhanced Biocompatibility of a Dry Adhesive Medical Skin Patch," *Advanced Materials*, vol. 23, p. 5, 2011.
- [36] S. N. Gorb and V. L. Popov, "Probabilistic fasteners with parabolic elements: biological system, artificial model and theoretical considerations," *Philosophical Transactions of the Royal Society of London Series a-Mathematical Physical and Engineering Sciences*, vol. 360, pp. 211-225, Feb 15 2002.
- [37] S. N. Gorb, "Evolution of the dragonfly head-arresting system," *Proceedings of the Royal Society of London Series B-Biological Sciences*, vol. 266, pp. 525-535, Mar 7 1999.
- [38] H. Ko, J. Lee, B. E. Schubert, Y. L. Chueh, P. W. Leu, R. S. Fearing, and A. Javey, "Hybrid Core-Shell Nanowire Forests as Self-Selective Chemical Connectors," *Nano letters*, vol. 9, pp. 2054-2058, May 2009.
- [39] Y. F. Mo, K. T. Turner, and I. Szlufarska, "Friction laws at the nanoscale,"

- Nature*, vol. 457, pp. 1116-1119, Feb 26 2009.
- [40] Y. Zheng, H. Bai, Z. Huang, X. Tian, F. Q. Nie, Y. Zhao, J. Zhai, and L. Jiang, "Directional water collection on wetted spider silk," *Nature*, vol. 463, pp. 640-643, 2010.
- [41] H. Bai, X. Tian, Y. Zheng, J. Ju, Y. Zhao, and L. Jiang, "Direction Controlled Driving of Tiny Water Drops on Bioinspired Artificial Spider Silks," *Advanced Materials*, vol. 22, pp. 5521-5525, 2010.
- [42] A. R. Parker and C. R. Lawrence, "Water capture by a desert beetle," *Nature*, vol. 414, pp. 33-34, Nov 01 2001.
- [43] L. Zhai, M. C. Berg, F. C. Cebeci, Y. Kim, J. M. Milwid, M. F. Rubner, and R. E. Cohen, "Patterned superhydrophobic surfaces: Toward a synthetic mimic of the Namib Desert beetle," *Nano letters*, vol. 6, pp. 1213-1217, Jun 2006.
- [44] Y. Zheng, X. Gao, and L. Jiang, "Directional adhesion of superhydrophobic butterfly wings," *Soft Matter*, vol. 3, pp. 178-182, 2007.
- [45] S. Reddy, E. Arzt, and A. del Campo, "Bioinspired surfaces with switchable adhesion," *Advanced Materials*, vol. 19, pp. 3833-3837, 2007.
- [46] M. K. Kwak, C. Pang, H. E. Jeong, H. N. Kim, H. Yoon, H. S. Jung, and K. Y. Suh, "Towards the Next Level of Bioinspired Dry Adhesives: New Designs and Applications," *Advanced Functional Materials*, vol. 21, p. 3606, 2011.
- [47] M. P. Murphy, B. Aksak, and M. Sitti, "Gecko-Inspired Directional and Controllable Adhesion," *Small*, vol. 5, pp. 170-175, 2009.
- [48] M. D. Bartlett, A. B. Croll, D. R. King, B. M. Paret, D. J. Irschick, and A. J. Crosby, "Biomimetics: Looking Beyond Fibrillar Features to Scale Gecko-Like Adhesion " *Advanced Materials*, vol. 24, pp. 994-994, 2012.
- [49] E. V. Gorb and S. N. Gorb, "The effect of surface anisotropy in the slippery zone of *Nepenthes alata* pitchers on beetle attachment," *Beilstein journal of nanotechnology*, vol. 2, p. 302, 2011.
- [50] H. F. Bohn and W. Federle, "Insect aquaplaning: *Nepenthes* pitcher plants capture prey with the peristome, a fully wettable water-lubricated

- anisotropic surface," *Proceedings of the National Academy of Sciences of the United States of America*, vol. 101, p. 14138, 2004.
- [51] B. Dean and B. Bhushan, "Shark-skin surfaces for fluid-drag reduction in turbulent flow: a review," *Philosophical Transactions of the Royal Society A: Mathematical, Physical and Engineering Sciences*, vol. 368, pp. 4775-4806, 2010.
- [52] J. Hazel, M. Stone, M. Grace, and V. Tsukruk, "Nanoscale design of snake skin for reptation locomotions via friction anisotropy," *Journal of Biomechanics*, vol. 32, pp. 477-484, 1999.
- [53] F. Xia and L. Jiang, "Bio-inspired, smart, multiscale interfacial materials," *Advanced Materials*, vol. 20, pp. 2842-2858, Aug 4 2008.
- [54] M. K. Kwak, H. E. Jeong, T. I. Kim, H. Yoon, and K. Y. Suh, "Bio-inspired slanted polymer nanohairs for anisotropic wetting and directional dry adhesion," *Soft Matter*, vol. 6, pp. 1849-1857, 2010.
- [55] M. J. Hancock, K. Sekeroglu, and M. C. Demirel, "Bioinspired Directional Surfaces for Adhesion, Wetting, and Transport," *Advanced Functional Materials*, vol. in press, 2012.
- [56] C. Pang, T. I. Kim, W. G. Bae, D. Kang, S. M. Kim, and K. Y. Suh, "Bioinspired Reversible Interlocker Using Regularly Arrayed High Aspect-Ratio Polymer Fibers," *Advanced Materials*, vol. 24, pp. 475-+, Jan 24 2012.
- [57] H. Shahsavan and B. X. Zhao, "Conformal Adhesion Enhancement on Biomimetic Microstructured Surfaces," *Langmuir*, vol. 27, pp. 7732-7742, Jun 21 2011.
- [58] S. Vajpayee, K. Khare, S. Yang, C. Y. Hui, and A. Jagota, "Adhesion Selectivity Using Rippled Surfaces," *Advanced Functional Materials*, vol. 21, pp. 547-555, 2011.
- [59] R. Kapadia, H. Ko, Y. L. Chueh, J. C. Ho, T. Takahashi, Z. Zhang, and A. Javey, "Hybrid core-multishell nanowire forests for electrical connector applications," *Applied Physics Letters*, vol. 94, p. 263110, 2009.
- [60] M. K. Kwak, H. E. Jeong, and K. Y. Suh, "Rational Design and Enhanced

- Biocompatibility of a Dry Adhesive Medical Skin Patch," *Advanced Materials*, vol. 23, p. 3949, 2011.
- [61] H. Ko, Z. Zhang, Y. L. Chueh, E. Saiz, and A. Javey, "Thermoresponsive Chemical Connectors Based on Hybrid Nanowire Forests," *Angewandte Chemie*, vol. 122, pp. 626-629, 2010.
- [62] H. Ko, Z. Zhang, Y. L. Chueh, J. C. Ho, J. Lee, R. S. Fearing, and A. Javey, "Wet and Dry Adhesion Properties of Self-Selective Nanowire Connectors," *Advanced Functional Materials*, vol. 19, pp. 3098-3102, 2009.
- [63] H. Ko, Z. X. Zhang, J. C. Ho, K. Takei, R. Kapadia, Y. L. Chueh, W. Z. Cao, B. A. Cruden, and A. Javey, "Flexible Carbon-Nanofiber Connectors with Anisotropic Adhesion Properties," *Small*, vol. 6, pp. 22-26, Jan 4 2010.
- [64] C. Pang, D. Kang, T. I. Kim, and K. Y. Suh, "Analysis of Preload-Dependent Reversible Mechanical Interlocking Using Beetle-Inspired Wing Locking Device," *Langmuir*, vol. 28, pp. 2181-2186, Jan 31 2012.
- [65] Y. Rahmawan, T. I. Kim, S. J. Kim, K. R. Lee, M. W. Moon, and K. Y. Suh, "Surface energy tunable nanohairy dry adhesive by broad ion beam irradiation," *Soft Matter*, vol. 8, pp. 1673-1680, 2012.
- [66] D. H. Kim, N. S. Lu, R. Ma, Y. S. Kim, R. H. Kim, S. D. Wang, J. Wu, S. M. Won, H. Tao, A. Islam, K. J. Yu, T. I. Kim, R. Chowdhury, M. Ying, L. Z. Xu, M. Li, H. J. Chung, H. Keum, M. McCormick, P. Liu, Y. W. Zhang, F. G. Omenetto, Y. G. Huang, T. Coleman, and J. A. Rogers, "Epidermal Electronics," *Science*, vol. 333, pp. 838-843, Aug 12 2011.
- [67] K. Takei, T. Takahashi, J. C. Ho, H. Ko, A. G. Gillies, P. W. Leu, R. S. Fearing, and A. Javey, "Nanowire active-matrix circuitry for low-voltage macroscale artificial skin," *Nature Materials*, vol. 9, pp. 821-826, Oct 2010.
- [68] D. J. Lipomi, M. Vosgueritchian, B. C.-K. Tee, S. L. Hellstrom, J. A. Lee, C. H. Fox, and Z. Bao, "Skin-like pressure and strain sensors based on transparent elastic films of carbon nanotubes," *Nature Nanotechnology*,

vol. 6, p. 5, 2011.

- [69] S. C. B. Mannsfeld, B. C. K. Tee, R. M. Stoltenberg, C. V. H. H. Chen, S. Barman, B. V. O. Muir, A. N. Sokolov, C. Reese, and Z. N. Bao, "Highly sensitive flexible pressure sensors with microstructured rubber dielectric layers," *Nature Materials*, vol. 9, pp. 859-864, Oct 2010.
- [70] T. Yamada, Y. Hayamizu, Y. Yamamoto, Y. Yomogida, A. Izadi-Najafabadi, D. N. Futaba, and K. Hata, "A stretchable carbon nanotube strain sensor for human-motion detection," *Nature Nanotechnology*, vol. 6, pp. 296-301, May 2011.
- [71] M. C. McAlpine, H. Ahmad, D. W. Wang, and J. R. Heath, "Highly ordered nanowire arrays on plastic substrates for ultrasensitive flexible chemical sensors," *Nature Materials*, vol. 6, pp. 379-384, May 2007.
- [72] T. Sekitani, Y. Noguchi, K. Hata, T. Fukushima, T. Aida, and T. Someya, "A rubberlike stretchable active matrix using elastic conductors," *Science*, vol. 321, pp. 1468-1472, Sep 12 2008.
- [73] D. H. Kim, J. H. Ahn, W. M. Choi, H. S. Kim, T. H. Kim, J. Z. Song, Y. G. Y. Huang, Z. J. Liu, C. Lu, and J. A. Rogers, "Stretchable and foldable silicon integrated circuits," *Science*, vol. 320, pp. 507-511, Apr 25 2008.
- [74] T. Someya, T. Sekitani, S. Iba, Y. Kato, H. Kawaguchi, and T. Sakurai, "A large-area, flexible pressure sensor matrix with organic field-effect transistors for artificial skin applications," *Proceedings of the National Academy of Sciences of the United States of America*, vol. 101, pp. 9966-9970, Jul 6 2004.
- [75] T. Someya, Y. Kato, T. Sekitani, S. Iba, Y. Noguchi, Y. Murase, H. Kawaguchi, and T. Sakurai, "Conformable, flexible, large-area networks of pressure and thermal sensors with organic transistor active matrixes," *Proceedings of the National Academy of Sciences of the United States of America*, vol. 102, pp. 12321-12325, Aug 30 2005.
- [76] S. P. Lacour, J. Jones, S. Wagner, T. Li, and Z. G. Suo, "Stretchable interconnects for elastic electronic surfaces," *Proceedings of the Ieee*, vol. 93, pp. 1459-1467, Aug 2005.

- [77] B. Z. Tian, T. Cohen-Karni, Q. Qing, X. J. Duan, P. Xie, and C. M. Lieber, "Three-Dimensional, Flexible Nanoscale Field-Effect Transistors as Localized Bioprobes," *Science*, vol. 329, pp. 830-834, Aug 13 2010.
- [78] C. Cochrane, V. Koncar, M. Lewandowski, and C. Dufour, "Design and development of a flexible strain sensor for textile structures based on a conductive polymer composite," *Sensors*, vol. 7, pp. 473-492, Apr 2007.
- [79] T. Dvir, B. P. Timko, M. D. Brigham, S. R. Naik, S. S. Karajanagi, O. Levy, H. W. Jin, K. K. Parker, R. Langer, and D. S. Kohane, "Nanowired three-dimensional cardiac patches," *Nature Nanotechnology*, vol. 6, pp. 720-725, Nov 2011.
- [80] T. Takahashi, K. Takei, A. G. Gillies, R. S. Fearing, and A. Javey, "Carbon Nanotube Active-Matrix Backplanes for Conformal Electronics and Sensors," *Nano Letters*, vol. 11, p. 6, 2011.
- [81] D. H. Kim, Y. S. Kim, J. Wu, Z. J. Liu, J. Z. Song, H. S. Kim, Y. G. Y. Huang, K. C. Hwang, and J. A. Rogers, "Ultrathin Silicon Circuits With Strain-isolation Layers and Mesh Layouts for High-Performance Electronics on Fabric, Vinyl, Leather, and Paper," *Advanced Materials*, vol. 21, pp. 3703-+, Sep 25 2009.
- [82] J. Ashmore, "Cochlear outer hair cell motility," *Physiological Reviews*, vol. 88, pp. 173-210, Jan 2008.
- [83] M. A. Wurbel, M. G. McIntire, P. Dwyer, and E. Fiebiger, "CCL25/CCR9 Interactions Regulate Large Intestinal Inflammation in a Murine Model of Acute Colitis," *Plos One*, vol. 6, Jan 25 2011.
- [84] K. J. Jang and K. Y. Suh, "A multi-layer microfluidic device for efficient culture and analysis of renal tubular cells," *Lab on a Chip*, vol. 10, pp. 36-42, 2010.
- [85] A. Akhmanova and A. S. Yap, "Organizing Junctions at the Cell-Cell Interface," *Cell*, vol. 135, pp. 791-793, Nov 28 2008.
- [86] S. Kawaguchi and D. T. W. Ng, "Sensing ER Stress," *Science*, vol. 333, pp. 1830-1831, Sep 30 2011.
- [87] C. Pang, T.-i. Kim, W. G. Bae, D. Kang, S. M. Kim, and K.-Y. Suh, "Bio-

- inspired Reversible Interlocker Using Regularly Arrayed High Aspect-Ratio Polymer Fibers," *Advanced Materials*, vol. 24, pp. 475-479, 2012.
- [88] S. J. Choi, H. N. Kim, W. G. Bae, and K. Y. Suh, "Modulus- and surface energy-tunable ultraviolet-curable polyurethane acrylate: properties and applications," *Journal of Materials Chemistry*, vol. 21, pp. 14325-14335, 2011.
- [89] H. Yoon, H. E. Jeong, T. I. Kim, T. J. Kang, D. Tahk, K. Char, and K. Y. Suh, "Adhesion hysteresis of Janus nanopillars fabricated by nanomolding and oblique metal deposition," *Nano Today*, vol. 4, pp. 385-392, Oct 2009.
- [90] C. Pang, D. Kang, T.-i. Kim, and K.-Y. Suh, "Analysis of preload-dependent reversible mechanical interlocking using beetle-inspired wing locking device," *Langmuir*, vol. 28, pp. 2181-2186, 2012.
- [91] U. Z. Tsuyoshi Sekitani, Hagen Klauk and Takao Someya, "Flexible organic transistors and circuits with extreme bending stability," *Nature Materials*, vol. 9, pp. 1015-1022, 2010.
- [92] Y. Lee, S. Bae, H. Jang, S. Jang, S. E. Zhu, S. H. Sim, Y. I. Song, B. H. Hong, and J. H. Ahn, "Wafer-Scale Synthesis and Transfer of Graphene Films," *Nano Letters*, vol. 10, pp. 490-493, Feb 2010.
- [93] K. M. B. Jansen, "Effect of pressure on electrical resistance strain gages," *Experimental Mechanics*, vol. 37, pp. 245-249, Sep 1997.
- [94] K. Salaita, P. M. Nair, R. S. Petit, R. M. Neve, D. Das, J. W. Gray, and J. T. Groves, "Restriction of Receptor Movement Alters Cellular Response: Physical Force Sensing by EphA2," *Science*, vol. 327, pp. 1380-1385, Mar 12 2010.
- [95] C. R. White and J. A. Frangos, "The shear stress of it all: the cell membrane and mechanochemical transduction," *Philosophical Transactions of the Royal Society B-Biological Sciences*, vol. 362, pp. 1459-1467, Aug 29 2007.
- [96] R. F. Krimm, B. M. Davis, C. J. Woodbury, and K. M. Albers, "NT3 expressed in skin causes enhancement of SA1 sensory neurons that leads to postnatal enhancement of Merkel cells," *Journal of Comparative*

- Neurology*, vol. 471, pp. 352-360, Apr 5 2004.
- [97] E. S. Dellon, R. Mourey, and A. L. Dellon, "Human Pressure Perception Values for Constant and Moving One-Point and 2-Point Discrimination," *Plastic and Reconstructive Surgery*, vol. 90, pp. 112-117, Jul 1992.
- [98] R. C. Hibbeler, *Statics and mechanics of materials*, SI ed.: Pearson Prentice Hall, 2004.
- [99] S. J. Choi, K. Y. Suh, and H. H. Lee, "Direct UV-replica molding of biomimetic hierarchical structure for selective wetting," *Journal of the American Chemical Society*, vol. 130, pp. 6312-6313, May 21 2008.

국문초록

본 논문은 자연계에 존재하는 기능성 미세 구조물에 대한 멀티스케일 분석을 통해 그 특성을 파악하고, 이를 활용한 새로운 개념의 체결형 건식 접착제 (인터락커: Interlocker)와 다기능 유연 센서에 대한 공학적 설계와 제조방법을 제시한다. 즉, 딱정벌레 날개 잠금 장치의 마이크로 구조물을 관찰하여 반데르 발스 힘 (Van der Waals force)에 의한 가역적 (Reversibility)이고 방향성 (Directionality)을 갖는 체결 (Interlocking)현상에 대한 메커니즘을 규명하고, 결합력의 크기를 예측해 제어하기 위한 재료적, 구조적 모델링을 통해 자연의 기능을 초월하는 체결형 건식 접착제와 초감도 다기능 유연 센서와 같은 초기능성 응용시스템을 구현하는데 그 의미와 중요성이 있다.

구체적으로, 본 논문에서는 날개가 접힐 때는 몸체와 걸날개면의 미세 섬모 배열이 반데르 발스 힘에 의해 상호 접촉하면서 안정적으로 결합하며, 날개를 펼칠 때에는 가장자리에서부터 방향성을 갖고 섬모가 분리되는 (벗겨냄: Peeling off) 방식을 가지는 딱정벌레의 날개 잠금 장치를 관찰하고, 여기에서 영감을 받아 기존의 벨크로형 (Hook&Loop)의 체결 방식과는 전혀 다른 새로운 개념의 체결형 건식 접착제를 제시하였다. 또한, 이를 구현하기 위해서 대면적 공정에 유리한 UV-경화성 폴리우레탄 계열의 고분자를 사용하여 다양한 종류의 마이크로/나노 구조물을 제작하여, 동일한 형태의 상하 두 개의 접착부재를 서로 결합시키는 방식으로 멀티스케일 설계와 제조의 방법을 제시하였다. 접착력 테스트 결과 고중형비 나노 구조물의 전단

접착력은 최대 $\sim 40 \text{ N/cm}^2$ 으로 측정되었고, 이는 현존하는 고분자 건식 접착제 중 최고의 수치에 해당된다. 또한 이러한 접착력 측정값들은 구조와 재료적 특성에 의존하는 미세 섬모들 간의 힘들의 상호작용과 섬모의 결합 가능성에 기반을 둔 간단한 수학적 모델과 잘 일치하는 것을 확인 할 수 있었다.

나아가, 본 논문은 이러한 가역적 체결장치의 예압 (프리로드: Preload)에 의존한 전단 접착력의 강도 변화를 분석하였다. 상하 각각의 마이크로 및 나노 섬모들간의 접촉되는 길이가 프리로드 ($0.1 \sim 10 \text{ N/cm}^2$)에 의존함에 따라 전체 전단 접착력과 상관 관계를 모델링 하였다. 즉, 결합된 섬모들 간의 반데르 발스 힘과 구조적 굽힘력 (Bending force)이 프리로드에 따라 변화하는 것을 이용하여, 섬모의 움직임 분석하고 전체 섬모의 밀도로부터 전단 접착력을 예측할 수 있음을 제시하였다.

다음으로, 본 논문은 딱정벌레 날개 잠금 장치의 굽어 있는 상하 미세 섬모간의 결합을 관찰하여, 비대칭적인 접촉 특성을 가진 건식 체결형 접착제의 연구에 관해 기술하였다. 진공 상태에서 대면적 이온빔 조사 (ion beam irradiation) 공정을 이용하여 고종횡비의 마이크로 및 나노 구조물의 굽은 정도를 조절 할 수 있으며, 최대 굽은각이 40° 이내인 다양한 마이크로 및 나노 구조들을 제작할 수 있었다. 이러한 굽은 구조의 나노 섬모로부터 굽은 방향으로 당겼을 때 최대 $\sim 60 \text{ N/cm}^2$, 굽은 방향과 반대 방향으로 당겼을 때 최소 $\sim 20 \text{ N/cm}^2$ 의 전단 접착력을 갖는 비대칭적이고 쌍방향성의 건식 체결형 접착제를 제작할 수 있었으며, 당기는 방향에 따른 비대칭 이력이 ~ 3 임을 확인 할 수 있었다. 이러한 현상을 간단한 이론적 모델을 통해

분석하였고, 실험 결과를 잘 뒷받침할 수 있음을 확인하였다.

마지막으로, 본 논문에서는 반데르 발스 힘에 의한 미세 고분자 섬모의 체결 현상을 기반으로 한 초감도의 유연한 피부 부착형 센서를 개발하여 새로운 센서의 개념과 이를 통한 다양한 응용 방법을 제시하였다. 즉, 기존에 보고된 피부 부착형 다기능 센서는 나노스케일의 여러 층의 복잡한 패터닝 (Patterning) 및 조합 (Assembly) 공정이 필요한 문제점을 가지고 있는 반면, 본 논문의 다기능 피부접착 센서는 상대적으로 간단한 나노섬모 체결 현상을 통해 미세한 기계적 자극들 (압력, 전단, 뒤틀림)을 실시간으로 모니터링할 수 있는 새롭고 효율적인 개념을 가지고 있다. 반데르 발스 힘에 의한 나노 구조물들 간의 기계적 체결 구조를 기반으로 전기적 특성을 얻기 위해 나노섬모와 기판에 백금 (플레티늄: platinum)을 나노스케일로 증착하였고, 상하 나노섬모 간의 간단한 조합과 PDMS (polydimethylsiloxane)의 박막 실링 (Sealing)을 통해 센서를 제작하였다. 또한, 금속 증착 시 간단히 마스크잉 (Masking)을 통하여 64 개의 픽셀 (Pixel)들로 공간 분할이 가능함을 보여주었다. 그 결과, 압력의 경우 최소 5 Pa 의 매우 미세한 힘을 감지할 수 있었으며, 표면 전단의 경우 최소 0.001N, 토션의 경우 0.0002 Nm 의 힘을 감지할 수 있었다. 이러한 힘의 변화를 저항 변화값과 센서의 물리적 변형률에 대한 실시간 모니터링을 통해 G.F.(Gauge Factor)값을 분석함으로써 세 가지 각기 다른 물리적인 힘을 구분해 낼 수 있었다. 즉, 본 연구에서는 미세한 물리적 외력 (압력, 전단, 뒤틀림)에 의해 발생하는 전기 저항의 선형적인 변화를 통해 미세 힘의 종류와 크기를 감지할 수 있음을 증명하였다. 또한, 본 연구의 실용적 응용이 가능함을 확인하기

위해 초소수성 표면이 코팅된 센서 위에서 20 μ l 의 물방울을 5 cm 높이에서 떨어뜨려 운동에너지에 의해 발생한 표면의 물리적인 힘의 변화를 모니터링하였으며, 더 나아가 맥박을 짚 수 있는 손목에 센서를 접촉하여 운동 전후의 맥박의 변화 및 혈관 압력의 차이를 관찰 할 수 있었다. 이러한 결과를 통해 본 연구가 정밀 기계적인 응용과 생체 신호를 관찰하는 의공학 분야 및 인공 피부 기술로의 응용에 사용될 수 있음을 보여주었다.

주요어: 생체모사 공학, 딱정벌레, 날개 잠금 장치, 가역적 결합체, 건식 접착제, 비대칭 결합, 나노 섬모, 스트레인 게이지 센서, 피부 부착형 디바이스.

학번: 2009-31247

감사의 글

“본 학위 논문은 다른 곳의 훌륭한 학자들과의 독립적인 연구를 위한 극히 부분적으로 충족된 논문임을 밝힙니다.”

칸트가 말하였듯 행복의 조건은 간단한 것 같습니다. 사랑하는 사람들, 하고 싶은 일들, 그리고 희망을 가지고 있다면 그 사람은 행복하다고 하는데, 저는 그 조건을 모두 갖추었다는 것을 본 논문을 마무리 하면서 깨닫게 되었습니다.

다른 사람들과 달리 조금 멀리 돌고 돌아서 박사학위를 받는 동안 안타까운 마음에 염려와 지원을 아끼지 않았던 부모님의 사랑에 가슴 깊이 감사의 말씀을 드리고 싶습니다. 또한, 항상 가까운 곳에서 응원해주던 누나와 매형, 그리고 조카들에게 고맙고 사랑한다고 말하고 싶습니다.

박사과정 동안, 연구의 밑그림과 방향부터 세밀한 부분까지 꼼꼼한 가르침과, 끊임없는 도전과 자신과의 싸움을 아낌없이 격려하고 지원해주신 서갑양 지도교수님께 어떻게 감사를 드려야 할지 모르겠습니다. 논문이 완성되기까지 따뜻한 관심과 지도를 주신 최만수 교수님, 안성훈 교수님, 유필진 교수님, 그리고 권성훈 교수님께도 감사의 말씀을 전합니다. 백지상태에서 연구의 첫발을 내디딜 수 있도록 가르침을 주신 성균관대 채희엽 교수님께 감사의 말씀을 전합니다. 무엇보다 소중한 연구를 전해주고 가르쳐준 선배이자 친구 김태일 박사에게도 항상 고마운 마음을 가지고 있고 뜻하는 바를 이루길 기원합니다.

논문을 준비하는 힘든 시간 동안 격려와 위로를 함께 나누어 준 연구실 후배 대식이와 번번히 선배의 힘든 일들을 도맡아준 상문이, 민성이, 병준이와 찬석이에게 감사의 말을 전합니다. 같이 연구를 하지는 않았지만 옆에서 많은 도움과 조언을 아끼지 않았고, 앞으로 가야 할 길의 표본이 되어준 여러 훌륭한 MBSL 선배님들께 깊이 감사 드립니다. 번번히 부족한 선배의 말을 따라준 여러 MBSL 후배들에게 많이 고맙고 응원의 글 남깁니다.

일면식도 없는 사람의 부탁에 바쁜 와중에도 귀중한 시간과 장비를 할애해 준 서울대 화학생물공학부 정남기 박사와 전기공학부 효기에게 고마운 마음을 남깁니다. 또한, 어려운 부탁을 흔쾌히 들어주어 좋은 결과를 공유했던 길용에게 고맙다고 말하고 싶습니다. 힘들 때 마다 바쁜 와중에도 멀리 달려와준 술친구 십년지기 고등학교 친구들과 대학친구들도 곁에 있어 고맙다고 전하고 싶습니다.

앞으로의 연구자의 길에 즐거움과 비전을 제시해준 지도교수님을 포함한 여러 훌륭하신 교수님들, 특히 고군분투했던 최종 논문의 가치를 높여주신 University of Illinois 의 J. Rogers 교수님께 이 자리를 빌려 감사의 말씀 전합니다.

마지막으로, 짧은 날 작은 인생의 여정 동안 ‘인내와 기다림’의 지혜를 가르쳐주신 하느님께 가슴 깊이 감사를 드리며, 사랑의 결실이 머지않아 이루어 지기를 기도하며 글을 마칩니다.

2012년 7월.

관악산 중턱 302 동에서